Integrated torque-vectoring and anti-roll moment distribution strategies based on optimal control: influence of model complexity and road curvature preview

Original
Integrated torque-vectoring and anti-roll moment distribution strategies based on optimal control: influence of model complexity and road curvature preview / Amer, N.H., Dalboni, M., Georgiev, P., Caponio, C., Tavernini, D., Gruber, P., Dhaens, M., Sorniotti, A.. - In: VEHICLE SYSTEM DYNAMICS. - ISSN 0042-3114. - 62:10(2024), pp. 2533-2566. [10.1080/00423114.2023.2296586]

Publisher:
Taylor & Francis

Published
DOI:10.1080/00423114.2023.2296586

Taylor & Francis
Taylor & Francis Group

Vehicle System Dynamics
International Journal of Vehicle Mechanics and Mobility

ISSN: (Print) (Online) Journal homepage: www.tandfonline.com/journals/nvsd20

Integrated torque-vectoring and anti-roll moment distribution strategies based on optimal control: influence of model complexity and road curvature preview

N. H. Amer, M. Dalboni, P. Georgiev, C. Caponio, D. Tavernini, P. Gruber, M. Dhaens & A. Sorniotti

To cite this article: N. H. Amer, M. Dalboni, P. Georgiev, C. Caponio, D. Tavernini, P. Gruber, M. Dhaens & A. Sorniotti (2024) Integrated torque-vectoring and anti-roll moment distribution strategies based on optimal control: influence of model complexity and road curvature preview, Vehicle System Dynamics, 62:10, 2533-2566, DOI: 10.1080/00423114.2023.2296586

To link to this article: https://doi.org/10.1080/00423114.2023.2296586

VEHICLE SYSTEM DYNAMICS
2024, VOL. 62, NO. 10, 2533–2566
https://doi.org/10.1080/00423114.2023.2296586

Integrated torque-vectoring and anti-roll moment distribution strategies based on optimal control: influence of model complexity and road curvature preview

N. H. Amer[a,b], M. Dalboni[a,c], P. Georgiev[a], C. Caponio[a], D. Tavernini[a], P. Gruber[a], M. Dhaens[d] and A. Sorniotti[e,a]

[a]Centre for Automotive Engineering, University of Surrey, Guildford, UK; [b]Centre for Defence Research and Technology (CODRAT), National Defence University of Malaysia, Kuala Lumpur, Malaysia; [c]Department of Engineering and Architecture, University of Parma, Parma, Italy; [d]Research Department, Tenneco Automotive, Sint-Truiden, Belgium; [e]Department of Mechanical and Aerospace Engineering (DIMEAS), Politecnico di Torino, Turin, Italy

ABSTRACT

Although the vehicle dynamics effects of variable anti-roll moment distribution actuated through active suspension systems are widely discussed in the literature, their model-based control has only been recently analysed, given the highly nonlinear nature of the involved dynamics. Moreover, the available studies do not discuss the trade-off between internal model complexity and controller performance, nor analyse the opportunities offered by vehicle connectivity, which enables the prediction of the steering angle and reference yaw rate profiles ahead. To address the gap, this paper introduces and assesses three optimal controllers for an electric vehicle with active suspensions, multiple powertrains, and a brake-by-wire system. The formulations are: (a) a gain scheduled output feedback linear quadratic regulator (OFLQR); (b) a nonlinear model predictive controller using a three-degree-of-freedom prediction model, without and with preview of the steering angle and reference yaw rate ahead, respectively referred to as NMPC-3 and NMPC-3-Pre; and (c) a nonlinear model predictive controller based on an eight-degree-of-freedom prediction model, referred to as NMPC-8 and NMPC-8-Pre depending on the absence or presence of preview. The results on an experimentally validated model show that: (i) NMPC-8 provides evident yaw rate tracking benefits with respect to (w.r.t) OFLQR and NMPC-3; and (ii) NMPC-8-Pre can bring $\sim 20\%$ yaw rate tracking improvement w.r.t. an optimally tuned NMPC-8 configuration.

ARTICLE HISTORY
Received 24 January 2022
Revised 4 December 2023
Accepted 12 December 2023

KEYWORDS
Torque-vectoring; nonlinear model predictive control; anti-roll moment distribution; prediction model; road curvature preview

1. Introduction

Electric vehicles (EVs) have been the subject of significant recent interest. Extensive literature investigates EVs with two powertrains per axle [1–4], enabling continuous control of the left-to-right wheel torque difference, i.e, the so-called torque-vectoring (TV) [5]. TV can shape the understeer characteristic in quasi-steady-state conditions, increase yaw and

CONTACT A. Sorniotti aldo.sorniotti@polito.it, a.sorniotti@surrey.ac.uk

sideslip damping during transients [5–7], and reduce energy consumption [8, 9]. TV can also be supported by the friction brakes, which are more and more frequently implemented through electro-hydraulic or electro-mechanical arrangements [10].

Moreover, modern vehicles are often equipped with semi-active and/or active suspensions, to reduce the body motions, in terms of pitch and roll angles as well as heave displacement, together with the respective rates and accelerations, which are induced by: (i) the traction, braking and cornering actions; and (ii) road irregularities. Controllable suspensions are a key factor for exploiting the benefits of next generation automated vehicles, to enable users to carry out activities during vehicle operation, which is not currently possible [11].

Another potential functionality of active suspensions is vehicle dynamics control through variable front-to-total anti-roll moment distribution [12]. Within an axle, the increase of anti-roll moment, and thus lateral load transfer, reduces the lateral force. Therefore, an increment of the front anti-roll moment increases understeer, while an increase of the rear anti-roll moment reduces understeer. Traditionally, given their intrinsic nonlinearity, anti-roll moment distribution controllers are empirically designed, and operate independently from direct yaw moment controllers, e.g. see [13] and [14]. A few papers attempt the design of nonlinear anti-roll moment distribution algorithms through the model in [12], including parabolic dependency of tyre cornering stiffness on vertical load, and linear dependency of lateral tyre force on slip angle, see the model predictive controller (MPC) in [15]. However, recent studies [16, 17] have demonstrated the low fidelity of such approximation. Therefore, Ricco et al. [16, 17] propose a linearised lateral axle force formulation for the model-based design of anti-roll moment distribution controllers, and apply it to proportional integral (PI) and H_∞ controllers.

In the context of integrated chassis control (ICC), see the overview in [18] and typical implementations in [19] and [20], several papers discuss algorithms for vehicles concurrently actuating direct yaw moment and anti-roll moment distribution. While most of the studies propose separate controllers for the two actuations [21–23], a few use integrated controllers. For example, in [24] Wang et al. present a nonlinear model predictive controller (NMPC) for in-wheel motors, rear-wheel-steering, and active suspension actuators. However, the active suspensions do not contribute to the cornering response enhancement. Similarly, the testing conditions of the linear time-varying MPC in [25] only involve maximum lateral accelerations of $\sim 4\,\text{m/s}^2$, in which suspensions have very limited impact on vehicle dynamics. In [26] Adireddy et al. present an MPC for ICC, with a prediction model using the simplified tyre model in [27], corresponding to a linear relationship between vertical tyre load and lateral tyre force variations, which could compromise its effectiveness for roll stiffness distribution control. The results highlight the benefits of roll angle control, but it is unclear whether the suspension contribution is used for yaw rate tracking. In [10] Dalboni et al. propose an NMPC considering the relevant power loss contributions; however, they do not analyse the effect of prediction model complexity on controller performance.

For ICC, MPC is a very suitable technique, since it enables multi-variable control based on multi-objective optimisation, including consideration of constraints. As ICCs typically require low implementation time steps, implicit MPC, which solves the optimal control problem on-line, has traditionally been affected by its computational demand. However, the improvement of automotive control hardware, and the development of computationally efficient solvers [28, 29], have recently made NMPC a feasible option [30].

In conventional MPCs for vehicle dynamics, the human or automated steering input and reference variables, e.g. the reference yaw rate, are kept constant along the prediction horizon. Hence, the MPC prediction is realistic only for very short horizons, and longer horizons do not automatically bring enhanced performance, as the controller cannot account for the likely future vehicle trajectory. Such limitation is going to disappear in the next generation of connected vehicles, in which accurate localisation, future road curvature mapping and V2X (vehicle-to-X) can feed the controllers with realistic profiles of the expected inputs ahead.

Very few vehicle dynamics control studies consider preview. For example, in [31] Yim presents a linear quadratic regulator (LQR) for rollover prevention through direct yaw moment and active suspension control. The steering input preview is obtained from the expected path, and represents a disturbance. In [32], the preview function assumes that the steering profile of the preceding vehicle is transmitted to the ego vehicle, which uses it as a preview signal within an LQR, neglecting the interaction between longitudinal and lateral tyre forces, and the effect of the anti-roll moment distribution. An NMPC for pre-emptive stability control has been proposed in [33], which considers the current vehicle position and road curvature information to predict the steering input and reference yaw rate profiles. However, the performance evaluation along obstacle avoidance tests focuses on the pre-emptive braking action.

In conclusion, the literature shows a gap on vehicle dynamics control with preview, as: (i) none of the preview implementations considers the effect of suspension control on the yaw rate response, or ICC for yaw rate tracking and sideslip angle limitation through multiple actuators; and (ii) the preview algorithms use simplified models, which limit the effective adoption of the relatively long prediction horizons that could maximise road preview effectiveness.

This study covers the gap with the following contributions:

- Novel computationally efficient output feedback LQR and NMPCs, referred to as OFLQR and NMPC-3, for integrated direct yaw moment and anti-roll moment distribution control, based on three-degree-of-freedom (3-DoF) vehicle models embedding lateral axle force formulations considering the lateral load transfers.
- Comparison of OFLQR, NMPC-3, and an NMPC, referred to as NMPC-8, based on an 8-DoF prediction model.
- Simulation-based proof-of-concept implementation and assessment of NMPCs with road preview, including sensitivity analysis on the effect of the prediction horizon parameters.

2. Simulation framework and control system architecture

The considered EV is the prototype of the Horizon 2020 European project EVC1000 [34]. The vehicle has direct drive in-wheel motors, a brake-by-wire system including front electro-hydraulic and rear electro-mechanical brakes, and an electro-hydraulic suspension system prototype by Tenneco, specifically designed for roll angle compensation and front-to-total anti-roll moment distribution control. The system generates the controllable active

Table 1. Main parameters of the case study EV.

Description	Symbol	Value	Unit
Total vehicle mass	m	2843	kg
Vehicle centre of gravity height	h_{CG}	0.63	m
Roll axis height at the longitudinal coordinate of the centre of gravity	h_{roll}	0.09	m
Front and rear track widths	b_F, b_R	1.66	m
Front semi-wheelbase	a_F	1.47	m
Rear semi-wheelbase	a_R	1.46	m
Wheel radius	R_w	0.37	m
Yaw mass moment of inertia	I_z	5291	kgm^2
Peak torque of individual in-wheel machine	$T_{em,max,ij}$	1500	Nm
Peak power of individual in-wheel machine	$P_{em,max,ij}$	141	kW

anti-roll moments through individual actuators at the corners, while appropriate valves provide passive damping force contributions. The vehicle parameters are in Table 1.

Figures 1(a,b) show the notations and sign conventions of the main variables, while Figure 1(c) reports the functional blocks of the simulation framework, implemented in Matlab-Simulink, and including:

- The driver model, which generates the steering wheel angle, δ_{sw}, and the accelerator and brake pedal positions, θ_{acc} and θ_{bk} (in percentage).
- The reference generator, which calculates the total torque demand, T_{dem}, and the reference yaw rate, r_{ref}, through nonlinear maps, depending on the driver inputs and vehicle speed. To provide a sport-oriented response, the considered r_{ref} map induces a significantly less understeering behaviour than the passive version of the vehicle. At each time step, the reference variables are transmitted as scalars to OFLQR. For NMPC-3 and NMPC-8, at each time step the reference generator outputs $\mathbf{S_y} = [\mathbf{y_{ref,0}}\mathbf{y_{ref,1}} \cdots \mathbf{y_{ref,N_h-1}}]$, i.e. the sequence of reference variable vectors, $\mathbf{y_{ref,k_h}}$, computed at discrete times along the prediction horizon t_h, where the integer k_h is the prediction step.
- The online parameter generator, which at each step outputs the sequence $\mathbf{S_p} = [\mathbf{p}_0\mathbf{p}_1 \cdots \mathbf{p}_{N_h-1}]$ of parameter vectors, $\mathbf{p_{k_h}}$, for discrete points along t_h, as required by NMPC-3 and NMPC-8, see Sections 4.2-4.4.
- The three integrated TV and anti-roll moment distribution controllers, i.e. OFLQR, NMPC-3, and NMPC-8. For the active suspension contribution, all controllers output the desired front-to-total anti-roll moment distribution ratio, f_{roll}. For the TV contribution, OFLQR and NMPC-3 generate a reference direct yaw moment, $M_{z,ext}$, as they embed single-track models, while NMPC-8, being based on a double-track model, directly produces the reference torque on each wheel, T_{ij}, where the subscript $i = F, R$ indicates the front or rear axle, and the subscript $j = L, R$ indicates the left- or right-hand side.
- The torque distribution block, which is used by OFLQR and NMPC-3 to generate T_{ij} from T_{dem} and $M_{z,ext}$.
- The suspension force distribution block, which computes the reference active suspension forces at the corners, indicated as $F_{act,ij}$, starting from: (i) the total active anti-roll moment contribution, $M_{AR,act,tot}$, which is calculated internally as a linear function of lateral acceleration a_y; and (ii) the f_{roll} value output by the selected control option.

- The brake blending function, which, for each corner, computes the reference in-wheel motor torque, $T_{em,ij}$, and the reference friction braking torque, $T_{bk,ij}$, to achieve T_{ij}, while prioritising regeneration over friction brake actuation.
- A high-fidelity vehicle simulation model, set up through the software package VSM by AVL, and interfaced with the control architecture in Simulink. The model accounts for the six DoFs (three translations and three rotations) of the sprung mass, the four DoFs related to the unsprung mass displacements, and the four DoFs associated with wheel rotations. Nonlinearities are included, e.g. in terms of coupling among the DoFs of the sprung mass, as well as bump stop and shock absorber characteristics. Suspension kinematics and compliances are considered, together with the nonlinear tyre behaviour, modelled through the Pacejka magic formula, including relaxation [35]. The dynamics of the electric powertrains and chassis actuators are simulated through pure time delays and transfer functions, based on experimental data from the suppliers. The model of the passive EV, i.e. without the controllers, has been experimentally validated in quasi-steady-state and transient conditions, see the results in Figure 2, and therefore is a reliable tool for control assessment. The validity of the following analyses is supported by the fact that the VSM model formulation is completely independent from those of the models for control design in Section 3.

3. Models for OFLQR design and NMPC prediction

3.1. Model for OFLQR design

The OFLQR formulation uses a linearised 3-DoF single-track vehicle model, see Figure 1, described by the following lateral force, yaw moment and roll moment balances, under the small angle approximation [36]:

$$\begin{aligned}
\dot{\beta} &= \frac{1}{mu}[F_{y,F} + F_{y,R}] - r \\
\dot{r} &= \frac{1}{I_z}[F_{y,F}a_F - F_{y,R}a_R + M_{z,ext}] \\
\ddot{\varphi} &= \frac{1}{I_x}\{m_s u[\dot{\beta} + r]d + m_s g d\varphi - M_{AR,pass,F} - M_{AR,pass,R} - M_{AR,act,F} - M_{AR,act,R}\}
\end{aligned} \tag{1}$$

where $\dot{\beta}$, $\dot{r}$, and $\ddot{\varphi}$ are the time derivatives of vehicle sideslip angle (β) and yaw rate (r), and the second time derivative of roll angle (φ); m and m_s are the total vehicle mass and sprung mass, considered, in a first approximation, to be the same; $F_{y,i}$ are the lateral axle forces, i.e. the sum of the tyre cornering forces on the same axle; u is the longitudinal component of vehicle velocity; the lateral acceleration a_y is approximated as $a_y \approx u[\dot{\beta} + r]$; I_z and I_x are the yaw and roll mass moments of inertia; $M_{z,ext}$ is the direct yaw moment of the TV system; $d = h_{CG_S} - h_{roll}$ is the distance between the centre of gravity of m_s and the roll axis, see Figure 1; g is the gravitational acceleration; $M_{AR,pass,F}$ and $M_{AR,pass,R}$ are the anti-roll moments of the front and rear passive suspension components, i.e. springs, anti-roll bars, and passive damping components; and $M_{AR,act,F}$ and $M_{AR,act,R}$ are the front and rear active anti-roll moments. In (1) and the remainder, '[]' and '{}' indicate a factor in a product, while '()' indicates a function.

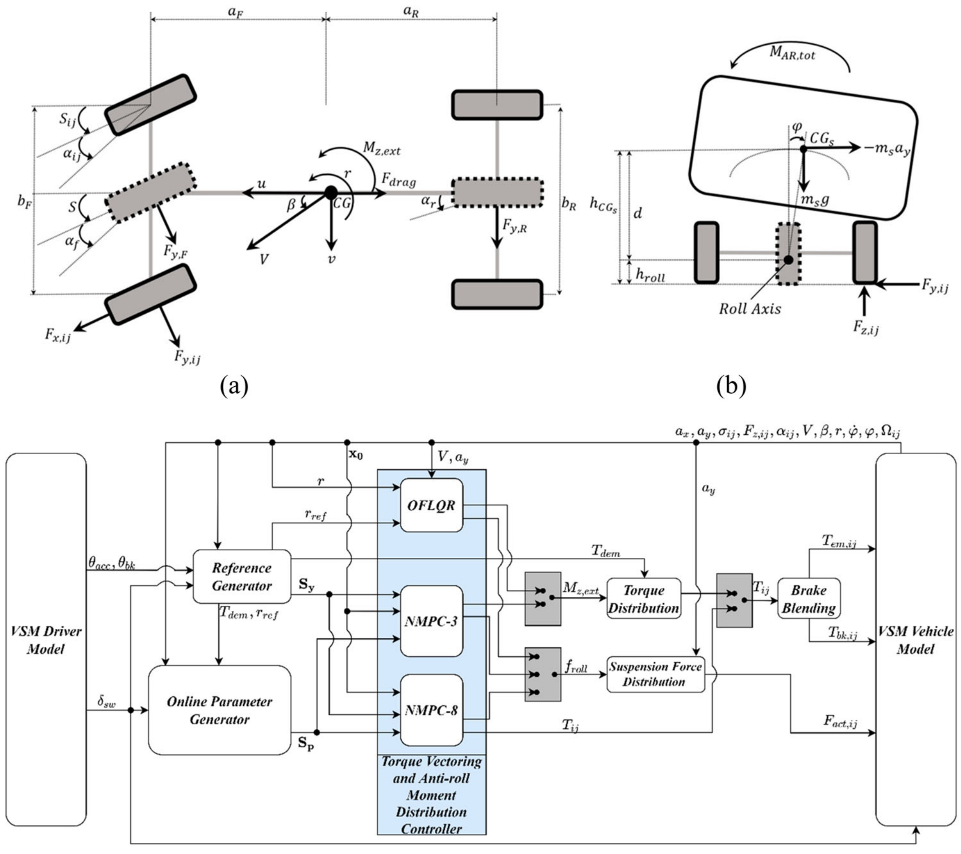

(a) (b)

(c)

Figure 1. Schematic of the vehicle model concepts for control design: (a) top view; (b) rear view. The dashed lines refer to the wheels of the single-track models of OFLQR and NMPC-3, and the continuous lines refer to the wheels of the double-track model of NMPC-8. (c) Simplified schematic of the simulation framework for the implementation and assessment of OFLQR, NMPC-3, and NMPC-8.

$M_{AR,pass,i}$ is approximated by the sum of linear stiffness and damping contributions [37]:

$$M_{AR,Pass,i} = K_{s,i}\varphi + D_i\dot{\varphi} \tag{2}$$

where $K_{s,i}$ is the roll stiffness of the passive components of the i axle suspension, and D_i is the roll damping coefficient. The roll moment balance allows considering the roll suspension dynamics in the lateral load transfer computation, while the suspension dynamics related to the pitch and heave motions are neglected to simplify the prediction model and enable real-time implementation. The total active anti-roll moment contribution, $M_{AR,act,tot} = M_{AR,act,F} + M_{AR,act,R}$, is the roll moment that is compensated by the active suspensions, and is expressed as a function of a_y, through $M_{AR,act,tot} = km_s a_y d$, where k is the roll motion compensation factor, i.e. $k = 1$ indicates full compensation, and $k = 0$ indicates absence of roll angle compensation. $M_{AR,act,tot}$ is distributed among the front and rear suspensions via the factor f_{roll} [17]:

$$M_{AR,act,F} = km_s a_y d f_{roll}$$

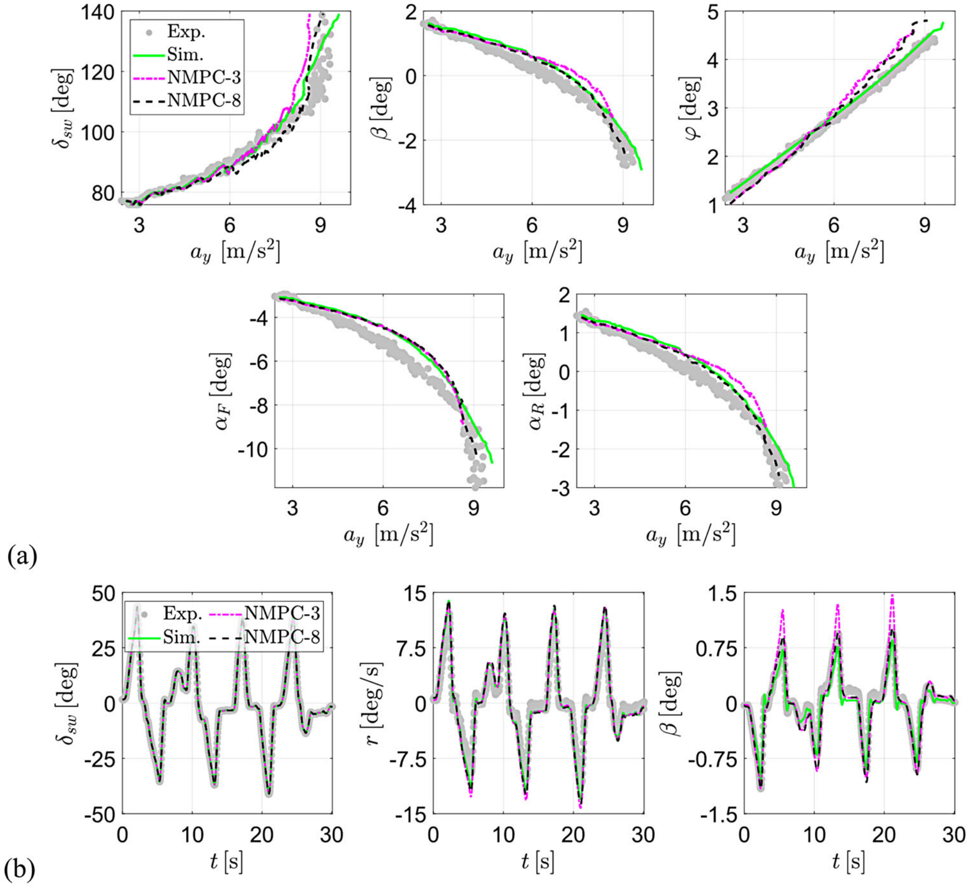

Figure 2. Examples of experimental validation of the considered models along: (a) a skidpad test, for which the steering wheel angle, δ_{sw}, sideslip angle, β, roll angle, φ, and front and rear axle slip angles, α_F and α_R, are reported as functions of the lateral acceleration, a_y; and (b) a transient steering manoeuvre at $\sim$ 100 km/h, along which the time profiles of δ_{sw}, yaw rate r, and β are reported. 'Exp.': experimental data; 'Sim.': simulation results from the VSM model; 'NMPC-3': simulation results from the prediction model of NMPC-3; and 'NMPC-8': simulation results from the prediction model of NMPC-8.

$$M_{AR,act,R} = k m_s a_y d[1 - f_{roll}] \tag{3}$$

Given the relatively slow nature of the yaw and roll motions, to reduce the computational load of the controllers, it was not deemed necessary to consider the suspension actuation dynamics in the prediction model. The lateral axle forces, $F_{y,i}$, are modelled through the formulation in [16] and [17], in which simplified relationships express the dependency of $F_{y,i}$ on the lateral load transfer, $\Delta F_{z,i}$, and slip angle, α_i, around a nominal operating condition defined by $F_{y,i,0}$, $\Delta F_{z,i,0}$, and $\alpha_{i,0}$, with the subscript '0' indicating the value of the variable at the considered nominal point:

$$F_{y,i} = F_{y,i,0} + F'_{y,i,0}[\Delta F_{z,i} - \Delta F_{z,i,0}] + \{C_{i,0} + C'_{i,0}[\Delta F_{z,i} - \Delta F_{z,i,0}]\}\,[\alpha_i - \alpha_{i,0}] \tag{4}$$

where $F'_{y,i,0} = \partial F_{y,i}/\partial \Delta F_{z,i}|_0$ is the gradient of the lateral axle force w.r.t. the lateral load transfer, which is always negative, as the magnitude of $F_{y,i}$ decreases with $\Delta F_{z,i}$; $C_{i,0}$ is the axle cornering stiffness at the nominal point, i.e. the slope of the lateral axle force characteristic as a function of slip angle; and $C'_{i,0} = \partial C_i / \partial \Delta F_{z,i}|_0$ is the gradient of the axle cornering stiffness w.r.t. the lateral load transfer, which, from [16] and [17], is usually negative for low values of $|\alpha_{i,0}|$, and positive for medium-to-high $|\alpha_{i,0}|$.

α_i is defined with the sign conventions in Figure 1 [37]:

$$\begin{aligned}
\alpha_F &= \beta + \frac{a_F}{u} r - S \\
\alpha_R &= \beta - \frac{a_R}{u} r
\end{aligned} \tag{5}$$

where S is the average front steering angle. The lateral load transfers are given by [37]:

$$\Delta F_{z,i} = \frac{m a_y [l - a_i] h_{roll}}{l b_i} + \frac{M_{AR,pass,i} + M_{AR,act,i}}{b_i} \tag{6}$$

where l is the wheelbase. By substituting (5) and (6) into (4), the lateral axle forces become:

$$\begin{aligned}
F_{y,F} &= F_{y,F,0} + F'_{y,F,0} \left\{ \frac{u[\dot{\beta} + r][m a_R h_{roll}/l + m_s k f_{roll} d] + K_F \varphi + D_F \dot{\varphi}}{b_F} - \Delta F_{z,F,0} \right\} \\
&\quad + \left\{ C_{F,0} + C'_{F,0} \left\{ \frac{u[\dot{\beta} + r][m a_R h_{roll}/l + m_s k f_{roll} d] + K_F \varphi + D_F \dot{\varphi}}{b_F} - \Delta F_{z,F,0} \right\} \right\} \\
&\quad \times \left[\beta + \frac{a_F}{u} r - S - \alpha_{F,0} \right] \\
F_{y,R} &= F_{y,R,0} \\
&\quad + F'_{y,R,0} \left\{ \frac{u[\dot{\beta} + r]\{m a_F h_{roll}/l + m_s k [1 - f_{roll}] d\} + K_R \varphi + D_R \dot{\varphi}}{b_R} - \Delta F_{z,R,0} \right\} \\
&\quad + \left\{ C_{R,0} + C'_{R,0} \left\{ \frac{u[\dot{\beta} + r]\{m a_F h_{roll}/l + m_s k [1 - f_{roll}] d\} + K_R \varphi + D_R \dot{\varphi}}{b_R} \right. \right. \\
&\quad \left. \left. - \Delta F_{z,R,0} \right\} \right\} \left[\beta - \frac{a_R}{u} r - \alpha_{R,0} \right]
\end{aligned} \tag{7}$$

Despite resulting from the linearisation in (4), the expressions in (7) are nonlinear, as they include products of the system states, e.g. β and r, by their time derivatives and/or the control inputs.

By combining (1)-(3) and (7), and making appropriate re-arrangements, the model assumes the form:

$$\begin{aligned}
\dot{\beta} &= g_1(\beta, r, \varphi, \dot{\varphi}, f_{roll}, M_{z,ext}) \\
\dot{r} &= g_2(\beta, r, \varphi, \dot{\varphi}, f_{roll}, M_{z,ext}) \\
\ddot{\varphi} &= g_3(\beta, r, \varphi, \dot{\varphi}, f_{roll}, M_{z,ext})
\end{aligned} \tag{8}$$

where g_1, g_2 and g_3 are nonlinear functions, detailed in the Appendix, see A.1-A.3. These are re-arranged to include the yaw rate error Δr ($\Delta r = r - r_{ref}$) among the states, by replacing r with $\Delta r + r_{ref}$. Therefore, the model is represented through a nonlinear state-space formulation:

$$\begin{aligned}\dot{\mathbf{x}} &= \mathbf{g}(\mathbf{x}, \mathbf{u})\\ \mathbf{y} &= \mathbf{h}(\mathbf{x}, \mathbf{u})\end{aligned} \tag{9}$$

where $\mathbf{x}$, $\mathbf{u}$ and $\mathbf{y}$ are the state, input, and output vectors:

$$\mathbf{x} = \begin{bmatrix} \beta \\ \Delta r \\ \varphi \\ \dot{\varphi} \end{bmatrix}; \ \mathbf{u} = \begin{bmatrix} f_{roll} \\ M_{z,ext} \end{bmatrix}; \ \mathbf{y} = [\Delta r] \tag{10}$$

For designing OFLQR, the model is further linearised about the considered nominal operating point, defined by the values $\mathbf{x}_0$, $\mathbf{u}_0$, and $\mathbf{y}_0$, while the variations of the system condition w.r.t. the linearisation point are indicated as $\delta\mathbf{x}$, $\delta\mathbf{u}$, and $\delta\mathbf{y}$. Hence, the vectors in (10) are expressed as $\mathbf{x} = \mathbf{x}_0 + \delta\mathbf{x}$, $\mathbf{u} = \mathbf{u}_0 + \delta\mathbf{u}$, and $\mathbf{y} = \mathbf{y}_0 + \delta\mathbf{y}$, while (9) becomes:

$$\begin{aligned}\delta\dot{\mathbf{x}} &= \mathbf{A}\delta\mathbf{x} + \mathbf{B}\delta\mathbf{u}\\ \delta\mathbf{y} &= \mathbf{C}\delta\mathbf{x} + \mathbf{D}\delta\mathbf{u}\end{aligned} \tag{11}$$

where $\mathbf{A}$, $\mathbf{B}$, $\mathbf{C}$, and $\mathbf{D}$ are the system state-space matrices, obtained through the symbolic computation software Maple. As the only considered output is Δr, it is $\mathbf{D} = 0$.

In the implementation, as suggested in [17] and [38], the linearisation point corresponds to steady-state cornering at $a_y = 9\ \text{m/s}^2$ (i.e. $F_{y,i}$, $F'_{y,i,0}$, $C_{i,0}$, and $C'_{i,0}$ are kept constant) for different values of u, which is considered a gain scheduling parameter.

3.2. NMPC-3 prediction model

NMPC-3 uses the 3-DoF nonlinear vehicle model in (A1)–(A3) as internal model. Although being nonlinear, the NMPC-3 model is based on the linearisation of the lateral axle force characteristics as functions of the lateral load transfer and slip angle, see (4) and (7), according to which the values of $F_{y,i,0}$, $F'_{y,i,0}$, $\Delta F_{z,i,0}$, $C_{i,0}$, $C'_{i,0}$, and $\alpha_{i,0}$ are fed into the controller as online data. Two methods were evaluated for obtaining the linearisation parameters during NMPC-3 operation:

- Online method. This method assumes the presence of an accurate on-board estimator of the states and variables for vehicle dynamics control, e.g. see [39] and [40], which can determine $F_{y,i,0}$, $\Delta F_{z,i,0}$, $\alpha_{i,0}$, as well as the tyre slip ratios $\sigma_{ij,0}$ and friction factors $\mu_{ij,0}$ (representative of the available tyre-road friction) at each time step. Given the focus of this research on the controllers, $F_{y,i,0}$, $\Delta F_{z,i,0}$, $\alpha_{i,0}$, $\sigma_{ij,0}$, and $\mu_{ij,0}$ are assumed to be known. $F'_{y,i,0}$, $C_{i,0}$, and $C'_{i,0}$ are computed online from their definitions:

$$F'_{y,i,0} = \frac{F_{y,i}(\alpha_{i,0}, \Delta F_{z,i,0} + \delta\Delta F_{z,i}) - F_{y,i,0}(\alpha_{i,0}, \Delta F_{z,i,0})}{\delta\Delta F_{z,i}}$$

$$C_{i,0}(\alpha_{i,0}, \Delta F_{z,i,0}) = \frac{F_{y,i}(\alpha_{i,0} + \delta\alpha_i, \Delta F_{z,i,0}) - F_{y,i,0}(\alpha_{i,0}, \Delta F_{z,i,0})}{\delta\alpha_i}$$

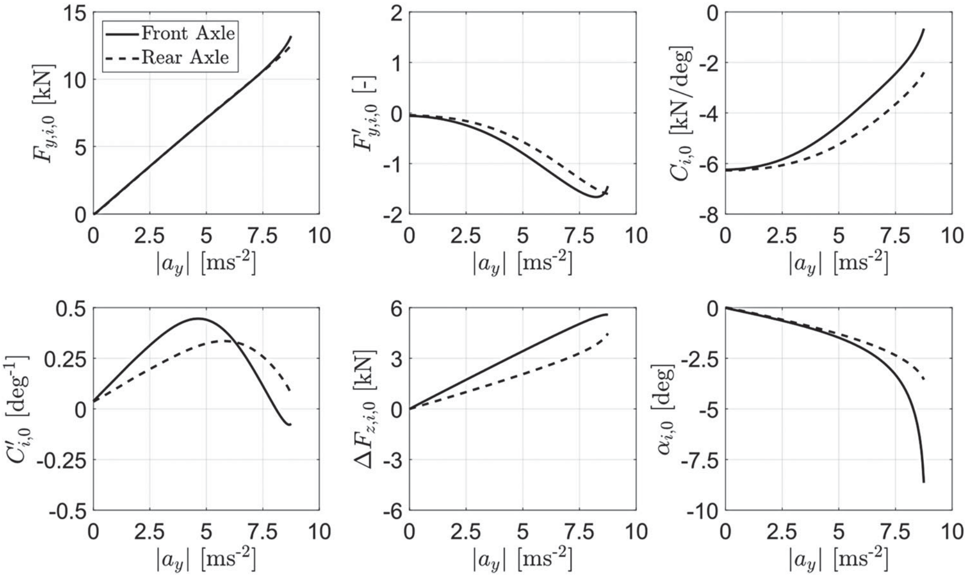

Figure 3. Examples of look-up tables for the generation of the axle force parameters for NMPC-3, in high tyre-road friction conditions.

$$C'_{i,0} = \frac{C_i(\alpha_{i,0}, \Delta F_{z,i,0} + \delta\Delta F_{z,i}) - C_{i,0}(\alpha_{i,0}, \Delta F_{z,i,0})}{\delta\Delta F_{z,i}} \tag{12}$$

where $\delta\Delta F_{z,i}$ and $\delta\alpha_i$ indicate small increments, respectively set to 500 N and 0.1 deg, of the lateral load transfer and slip angle w.r.t. their linearisation values. The lateral axle forces in (12), $F_{y,i}(\alpha_i, \Delta F_{z,i})$, are obtained online through version 5.2 of the magic formula [35], as the sum of the lateral tyre forces ($F_{y,ij}$) within the axle, by neglecting the steering angle difference among the two wheels:

$$F_{y,i}(\alpha_i, \Delta F_{z,i}) \approx F_{y,iR}(\alpha_{iR}, \sigma_{iR,0}, F_{z,iR}, L_{\mu max,ij,0}) + F_{y,iL}(\alpha_{iL}, \sigma_{iL,0}, F_{z,iL}, L_{\mu max,ij,0}) \tag{13}$$

where $L_{\mu max,ij,0}$ is the scaling factor of the tyre-road friction level in the Pacejka model.

- Offline method. This method uses the high-fidelity simulation model in quasi-steady-state conditions (ramp steer test), in conjunction with the offline implementation of (12) and (13), to obtain maps of $F_{y,i,0}$, $F'_{y,i,0}$, $C_{i,0}$, $C'_{i,0}$, $\Delta F_{z,i,0}$, and $\alpha_{i,0}$ as functions of $|a_y|$, see Figure 3 for high tyre-road friction conditions. The maps are then embedded in the online algorithm. The benefit is a significant reduction of the computational load for online estimation, at the price of neglecting the effects of driving transients, disturbances and model mismatches, which can be considered by the online method, see the critical analysis of this aspect for TV systems in [38].

3.3. Prediction model of NMPC-8

NMPC-8 uses a double-track 8-DoF prediction model, see Figure 1. The model includes the longitudinal force, lateral force, yaw moment, roll moment, and individual wheel moment balance equations in [10]. The tyre model, based on a simplified version of the magic formula, considers the interaction between longitudinal and lateral tyre forces, $F_{x,ij}$ and $F_{y,ij}$. The formulation makes the nonlinear lateral tyre force characteristic quadratically dependent on the load, to consider the effect of the lateral load transfer, and thus the front-to-total anti-roll moment distribution, on the lateral axle forces. The individual tyre load, $F_{z,ij}$, is obtained as the sum of the static load, and the longitudinal and lateral load transfers.

4. Controller configurations

4.1. OFLQR formulation

The linear quadratic formulation uses output feedback, which enables a simple control law, exclusively focused on the yaw rate error Δr, and does not rely on the continuous and accurate estimation of other states. Moreover, an integral yaw rate error contribution enables steady-state error compensation. The proportional integral (PI) OFLQR design proposed in [41] was selected, with a control law of the form:

$$\mathbf{u}(t) = -\mathbf{K_p}\mathbf{y}(t) - \mathbf{K_i}\int_0^t \mathbf{y}(t)dt \tag{14}$$

where t is time, and $\mathbf{K_p}$ and $\mathbf{K_i}$ are the gain matrices. For ease of notation, the symbol 'δ' is omitted from the variables in (14) and the remainder. For the system in (11), the objective of the OFLQR control law is to minimise the cost function J_{OFLQR}:

$$J_{OFLQR} = \int_0^\infty [\mathbf{x}(t)^T\mathbf{Q}\mathbf{x}(t) + \mathbf{u}(t)^T\mathbf{R}\mathbf{u}(t)]dt \tag{15}$$

where $\mathbf{Q}$ and $\mathbf{R}$ are diagonal weight matrices. To enable meaningful weight selection, the matrices $\mathbf{A}$, $\mathbf{B}$ and $\mathbf{C}$ in (11) were scaled through diagonal matrices including the maximum expected magnitudes of the states, control inputs, and outputs, which were quantified through VSM simulations. $\mathbf{Q}$ and $\mathbf{R}$ were selected to prioritise yaw rate tracking, with equal penalty on the TV and anti-roll moment distribution control effort.

$\mathbf{K_p}$ and $\mathbf{K_i}$ are obtained by solving the optimisation in [41], including linear matrix inequalities, for the model linearisation conditions in Section 3.1, i.e. for several vehicle speeds, covering the whole relevant range, at a lateral acceleration of 9 m/s^2. Differently from the NMPCs, OFLQR does not consider system constraints, while the control inputs are saturated according to the actuation capabilities. The gain maps as functions of speed are stored in the online algorithm of the controller, and the gain values are interpolated w.r.t. the current vehicle speed. Although formal stability proof of the weight scheduling algorithm is not provided, extensive simulations – see Section 5 – verified robustness and stability. As discussed in [16], in the online implementation, Δr is the error variable for the computation of $M_{z,ext}$, while Δr sign (r_{ref}) is the error variable for the computation of f_{roll}. Appropriate reset conditions, based on the reference yaw rate, reference yaw acceleration, and measured lateral acceleration, are used for the integral term.

4.2. NMPC-3 formulation

The nonlinear optimal control problem (NOCP) of NMPC-3 minimises the cost function J_{NMPC-3}, subject to the set of equality and inequality constraints (i)-(x):

$$\begin{aligned}
&J_{NMPC-3}(\mathbf{x}_0, \mathbf{u}(t), \mathbf{p}) \\
&\quad = \int_0^{t_h} \|\mathbf{y}(t) - \mathbf{y_{ref}}\|^2_{\mathbf{w}} dt + \|\mathbf{y}(t_h) - \mathbf{y_{ref}}\|^2_{\mathbf{w_f}} \\
&\quad = \int_0^{t_h} \|[\Delta r(t)\ \alpha_R(t)\ \Delta f_{roll}(t)\ M_{z,ext}(t)\ z_{\alpha_F}(t)\ z_{\alpha_R}(t)]^T\|^2_{\mathbf{w}} dt + w_f \Delta r(t_h)^2 \\
&s.t. \\
&(\text{i})\dot{\mathbf{x}} = \mathbf{g}(\mathbf{x}, \mathbf{u}, \mathbf{p}) \\
&(\text{ii})\mathbf{y} = \mathbf{h}(\mathbf{x}, \mathbf{u}, \mathbf{p}) \\
&(\text{iii})M_{z,ext,min} \leq M_{z,ext} \leq M_{z,ext,max} \\
&(\text{iv})f_{roll,min} \leq f_{roll} \leq f_{roll,max} \\
&(\text{v})|M_{AR,act,F}| \leq M_{AR,act,F,max} \\
&(\text{vi})|M_{AR,act,R}| \leq M_{AR,act,R,max} \\
&(\text{vii})\alpha_{F,min} - z_{\alpha_F} \leq \alpha_F \leq \alpha_{F,max} + z_{\alpha_F} \\
&(\text{viii})\alpha_{R,min} - z_{\alpha_R} \leq \alpha_R \leq \alpha_{R,max} + z_{\alpha_R} \\
&(\text{ix})z_{\alpha_F} \geq 0 \\
&(\text{x})z_{\alpha_R} \geq 0
\end{aligned} \tag{16}$$

The NOCP uses the nonlinear state-space form of the prediction model in (A.1)-(A.3) and Sections 3.1 and 3.2, see equality constraints (i) and (ii) in (16). The prediction is based on the initial values of the system state vector $\mathbf{x}_0$, the sequence of control inputs $\mathbf{u}(t)$, and the external parameter vector $\mathbf{p}(t)$, where t indicates the time along the prediction horizon t_h. The state vector is $\mathbf{x}(t) = [\beta\ r\ \varphi\ \dot{\varphi}]^T$, while the control input vector $\mathbf{u}(t)$, in addition to the active suspension and TV control actions, includes the slack variables, z_{α_F} and z_{α_R}, associated with the soft constraints, i.e. $\mathbf{u}(t) = [f_{roll}\ M_{z,ext}\ z_{\alpha_F}\ z_{\alpha_R}]^T$.

J_{NMPC-3} is quadratic, and is the sum of:

- A first term, $\int_0^{t_h} \|\mathbf{y}(t) - \mathbf{y_{ref}}\|^2_{\mathbf{w}} dt$, resulting from the integration of the weighted and squared 2-norm of the error (the so-called stage cost) between the output vector, $\mathbf{y}$, generated by the prediction model, and the reference output vector, $\mathbf{y_{ref}}$, along t_h. The priority level of each term of $\mathbf{y}(t) - \mathbf{y_{ref}}$ is governed by a diagonal weight matrix, $\mathbf{w}$. As $\mathbf{y}$ and $\mathbf{y_{ref}}$ are vectors consisting of several components, the norm of $\mathbf{y}(t) - \mathbf{y_{ref}}$ can also be expressed as the one of its individual components, i.e. the error values of the system outputs. Whilst for the yaw rate and anti-roll moment distribution factor the reference value is non-zero, which corresponds to the error variables $\Delta r(t)$ and $\Delta f_{roll}(t)$, the reference values of the rear axle slip angle, direct yaw moment, and slack variables are zero, and thus the respective error terms simplify into $\alpha_R(t)$, $M_{z,ext}(t)$, $z_{\alpha_F}(t)$, and $z_{\alpha_R}(t)$. As a summary, the first term of J_{NMPC-3} consists of contributions penalising: (a) Δr, which is the main focus; (b) α_R, to facilitate vehicle stabilisation; (c) the front-to-total anti-roll moment distribution control effort, expressed through the deviation, Δf_{roll}, of f_{roll} from its nominal value $f_{roll,nom}$, i.e. $\Delta f_{roll} = f_{roll} - f_{roll,nom}$, where $f_{roll,nom} = 0.67$ is the front-to-total anti-roll moment distribution factor of the corresponding vehicle without active suspension; (d) the TV control effort, $M_{z,ext}$; (e) the slack variable z_{α_F}, which sets a soft constraint on α_F, preventing excessive understeer, see also (vii) and (ix) in (16), where $\alpha_{F,min}$ and $\alpha_{F,max}$ are the lower and upper activation thresholds of the constraint; and (f) the slack variable, z_{α_R}, that sets a soft constraint on α_R, to prevent oversteer, see also (viii) and (x) in (16), defining the lower and upper limits $\alpha_{R,min}$ and $\alpha_{R,max}$. The minimisation of the positive slack variables z_{α_F} and z_{α_R} in the NMPC-3 cost function tends to push back α_F and α_R towards $\alpha_{F,max}$ and $\alpha_{R,max}$ as soon as the predicted slip angle values exceed their respective thresholds, and, similarly, to push back α_F and α_R toward $\alpha_{F,min}$ and $\alpha_{R,min}$ if the angle predictions go below their negative thresholds. This creates a constraint effect, referred to as soft, as the involved variable can cross their thresholds. The benefit of soft constraints instead of hard constraints is an easier convergence of the algorithm (infeasibility prevention), together with a reduction of the computational load.

- A second term, $\|\mathbf{y}(t_h) - \mathbf{y_{ref}}\|^2_{\mathbf{w_f}}$, the so-called terminal cost, accounting for the norm of $\mathbf{y} - \mathbf{y_{ref}}$ at the end of the prediction horizon, to facilitate controller stability through convergence of the outputs towards the respective reference. In the specific formulation, the terminal cost only considers the final magnitude of Δr, and the weight matrix $\mathbf{w_f}$ simplifies into a scalar, w_f.

In addition to the constraints in (i)–(ii) and (vii)–(x), (16) also includes: constraint (iii), which sets hard bounds, $M_{z,ext,min}$ and $M_{z,ext,max}$, for the direct yaw moment; constraint (iv), which sets the lower and upper bounds, $f_{roll,min}$ and $f_{roll,max}$, respectively 0.2 and 0.8, for f_{roll}, according to the available active suspension system, and to prevent extreme anti-roll moment distributions; and constraints (v) and (vi), limiting the magnitudes of the front and rear anti-roll moments to be less than $M_{AR,act,F,max}$ and $M_{AR,act,R,max}$.

In (16), the NOCP is in its continuous form, as this is the one for coding the controllers in the selected implementation tool, which carries out the discretisation along t_h, according to N_h steps, such that $t_h = N_h T_s$, where T_s is the prediction step. As shown in Figure 1, the NOCP requires the computation or estimation, outside the NMPC, of: (a) the vector with the initial values of the states, $\mathbf{x}_0$; (b) the vector $\mathbf{S_y}$ with the sequence of reference vectors, $\mathbf{y_{ref,k_h}}$, along t_h; and (c) the vector $\mathbf{S_p}$ with the sequence of parameter vectors, $\mathbf{p_{k_h}}$. For the NMPC-3 and NMPC-8 versions without preview, the reference and parameter vectors within the sequence are identical, i.e. $\mathbf{y_{ref,0}} = \mathbf{y_{ref,1}} = \ldots = \mathbf{y_{ref,N_h-1}} = \mathbf{y_{ref}}$ and $\mathbf{p}_0 = \mathbf{p}_1 = \ldots = \mathbf{p}_{N_h-1} = \mathbf{p}$, consistently with the current practice of MPC for vehicle chassis control. For NMPC-3, $\mathbf{y_{ref}}$ and $\mathbf{p}$ are:

$$\begin{aligned} \mathbf{y_{ref}} &= [r_{ref}\ 0\ f_{roll,nom}\ 0\ 0\ 0]^T \\ \mathbf{p} &= [S\ V\ a_y\ k\ M_{AR,act,F,max}\ M_{AR,act,R,max}\ f_{roll,min}\ f_{roll,max}\ M_{z,min}\ M_{z,max} \\ &\quad \alpha_{F,min}\ \alpha_{R,min}\ \alpha_{F,max}\ \alpha_{R,max}\ \Delta F_{z,F,0}\ \Delta F_{z,R,0}\ \alpha_{F,0}\ \alpha_{R,0}\ F_{y,F,0}\ F_{y,R,0}\ F'_{y,F,0} \\ &\quad F'_{y,R,0}\ C_{F,0}\ C_{R,0}\ C'_{F,0}\ C'_{R,0}]^T \end{aligned} \tag{17}$$

In NMPC-3, and the following NMPC-8, the a_y value in $\mathbf{p}$, e.g. used for the computation of the total active anti-roll moment and lateral load transfers, is the one measured by the sensor installed on the vehicle, i.e. $a_y = a_{y,meas}$.

4.3. NMPC-8 formulation

The NMPC-8 formulation is similar to the one in [10], with an NOCP having the same structure as for NMPC-3:

$$\begin{aligned}
&J_{NMPC-8}(\mathbf{x}_0, \mathbf{u}(t), \mathbf{p}) = \int_0^{t_h} \| [\Delta T_{tot}(t)\ e_r(t)\ P_{brakes}(t)\ \Delta T_{f,L}(t)\ \Delta T_{f,R}(t)\ \Delta f_{roll}(t) \\
&z_\sigma(t)\ z_{\alpha_F}(t)\ z_{\alpha_R}(t)]^T \|^2_{\mathbf{w}} dt + w_f e_r(t_h)^2 \\
&s.t. \\
&(\text{i})\ \dot{\mathbf{x}} = \mathbf{g}(\mathbf{x}, \mathbf{u}, \mathbf{p}) \\
&(\text{ii})\ \mathbf{y} = \mathbf{h}(\mathbf{x}, \mathbf{u}, \mathbf{p}) \\
&(\text{iii})\, T_{em,min,ij} + T_{bk,min,ij} \le T_{ij} \le T_{em,max,ij} \\
&(\text{iv})\, T_{FL} + T_{FR} \le k_{EBD} \sum T_{ij} \\
&(\text{v})\ \sum T_{em,ij} \le T_{tot,max} \\
&(\text{vi})\ \sum T_{ij} \ge T_{tot,min} \\
&(\text{vii})\, f_{roll,min} \le f_{roll} \le f_{roll,max} \\
&(\text{viii})\, |M_{AR,act,F}| \le M_{AR,act,F,max} \\
&(\text{ix})\, |M_{AR,act,R}| \le M_{AR,act,R,max} \\
&(\text{x})\, \sigma_{min} - z_\sigma \le \sigma_{ij} \le \sigma_{max} + z_\sigma \\
&(\text{xi})\, \alpha_{F,min} - z_{\alpha_F} \le \alpha_{Fj} \le \alpha_{F,max} + z_{\alpha_F} \\
&(\text{xii})\, \alpha_{R,min} - z_{\alpha_R} \le \alpha_{Rj} \le \alpha_{R,max} + z_{\alpha_R} \\
&(\text{xiii})\, z_\sigma \ge 0 \\
&(\text{xiv})\, z_{\alpha_F} \ge 0 \\
&(\text{xv})\, z_{\alpha_R} \ge 0
\end{aligned} \tag{18}$$

Constraints (i) and (ii) correspond to the 8-DoF model in Section 3.3, used for the prediction. $\mathbf{x}(t)$ and $\mathbf{u}(t)$ are:

$$\mathbf{x}(t) = [V\ \beta\ r\ \dot{\varphi}\ \varphi\ \Omega_{FL}\ \Omega_{FR}\ \Omega_{RL}\ \Omega_{RR}\ e_{int,r}]^T \tag{19}$$

$$\mathbf{u}(t) = [T_{FL}\ T_{FR}\ T_{RL}\ T_{RR}\ f_{roll}\ z_\sigma\ z_{\alpha_F}\ z_{\alpha_R}]^T \tag{20}$$

where $e_{int,r}$ is the time integral of the yaw rate error, i.e. $e_{int,r} = \int \Delta r(t) dt$.

The first term of J_{NMPC-8}, whose magnitude has to be minimised, consists of weighted quadratic contributions, corresponding to the following variables:

- ΔT_{tot}, which governs the tracking of total torque demand, T_{dem}, at the vehicle level:

$$\Delta T_{tot} = \sum_{i=F,R} \sum_{j=L,R} [T_{ij} - T_{dem}] \tag{21}$$

- e_r, which governs the tracking of r_{ref}, and is the linear combination of Δr and $e_{int,r}$, with weighting coefficient k_{int}:

$$e_r = \Delta r + k_{int} e_{int,r} \tag{22}$$

- P_{brakes}, i.e. the power dissipated within the friction brakes, which is considered to reduce their intervention:

$$P_{brakes} = \sum_{i=F,R} \sum_{j=L,R} [-T_{bk,ij} \Omega_{ij}] \tag{23}$$

- $\Delta T_{f,L}$ and $\Delta T_{f,R}$, auxiliary wheel torque values expressing the deviation of the front-to-total electric motor torque distributions on the left and right vehicle sides from their reference values, defined by the optimal reference of front-to-total torque distribution ratios, $f_{T,L,opt}$ and $f_{T,R,opt}$:

$$\Delta T_{f,L} = |T_{em,FL} [f_{T,L,opt} - 1] + T_{em,RL} f_{T,L,opt}| \tag{24}$$

$$\Delta T_{f,R} = |T_{em,FR} [f_{T,R,opt} - 1] + T_{em,RR} f_{T,L,opt}| \tag{25}$$

  The $f_{T,j,opt}$ values are computed offline to minimise the powertrain power losses on the j side, for each combination of motor speed and total electric motor torque demand on the side, $T_{em,tot,side,j}$, see [10] and [30].
- Δf_{roll}, see NMPC-3.
- z_σ, z_{α_F}, and z_{α_R}, which are the slack variables defining the soft constraints on the slip ratios and slip angles, i.e. σ_{ij}, α_{Fj}, and α_{Rj}.

With respect to the constraints in (18), (iii) sets the upper and lower bounds for each wheel torque, based on the actuation limits of the in-wheel motors and friction brakes; (iv) imposes a front-to-total braking torque distribution limitation, according to the coefficient k_{EBD}, computed by an external electronic brake distribution algorithm, and provided to NMPC-8 as an external parameter; (v) and (vi) set lower and upper bounds, $T_{tot,min}$ and $T_{tot,max}$, on the total torque; (vii)–(ix) deal with the active suspension actuation, similarly to the corresponding constraints of NMPC-3; (x)–(xii) define soft constraints for the longitudinal slip ratio of each tyre, and the front and rear slip angles; finally, (xiii)–(xv) ensure positive values of the slack variables.

$\mathbf{y_{ref}}$ and $\mathbf{p}$ are:

$$\begin{aligned} \mathbf{y_{ref}} &= [T_{dem}\ 0\ 0\ 0\ 0\ f_{roll,nom}\ 0\ 0\ 0] \\ \mathbf{p} &= [S_{FL}\ S_{FR}\ S_{RL}\ S_{RR}\ r_{ref}\ a_x\ a_y\ k\ k_{int}\ k_{EBD}\ \sigma_{max}\ \alpha_{F,max}\ \alpha_{R,max}\ \sigma_{min} \\ &\quad \alpha_{F,min}\ \alpha_{R,min}\ T_{em,min,FL}\ T_{em,min,FR}\ T_{em,min,RL}\ T_{em,min,RR} \\ &\quad T_{em,max,FL}\ T_{em,max,FR}\ T_{em,max,RL} \\ &\quad T_{em,max,RR}\ f_{T,L,opt}\ f_{T,R,opt}\ M_{AR,Act,F,max}\ M_{AR,Act,R,max}\ f_{roll,min}\ f_{roll,max} \end{aligned}$$

$$T_{tot,max}\ T_{tot,min}\ L_{\mu max}]^T \tag{26}$$

Similarly to a_y, in (26) also a_x is constant along t_h, and equal to the vehicle accelerometer output, i.e. $a_x = a_{x,meas}$. In the NMPC-8 coding, r_{ref} is in $\mathbf{p}$ instead of $\mathbf{y_{ref}}$, since it is needed in the computation of the integral term of e_r.

4.4. NMPC formulations with preview

For the NMPCs in Sections 4.2 and 4.3, this study evaluates the benefits of preview control. In fact, thanks to V2X, it will be possible to know the steering angle profile in advance, either through information from preceding vehicles, or the knowledge of the expected trajectory curvature, based on reasonable assumptions. Thus, the expected future steering input can be provided along t_h as a preview, and used in the internal model for predicting vehicle response. Moreover, as the reference yaw rate depends on the steering input, also its profile, under reasonable assumptions, i.e. constant vehicle speed or acceleration along the prediction, can be obtained, thus achieving a second source of preview. Hence, in the preview-based NMPCs, S_{Fj} and r_{ref} vary along the prediction, i.e. $S_{Fj}(k_h)$ and $r_{ref}(k_h)$.

In the preview formulations, two options were considered for the lateral acceleration for the computation of $M_{AR,act,tot}$ and $\Delta F_{z,i}$:

- Using the constant $a_{y,meas}$ value, as for the formulations without preview, which is simple and computationally efficient.
- Considering a variable $a_y(k_h)$ profile, according to the following empirical formulation:

  $$a_{y,var}(k_h) = w_{a_y}(k_h)a_{y,meas} + [1 - w_{a_y}(k_h)]r_{ref}(k_h)V_{est} \tag{27}$$

  where V_{est} is the currently estimated vehicle speed; and the weight w_{a_y} linearly decreases from 1 to 0 with increasing k_h:

  $$w_{a_y}(k_h) = 1 - \frac{k_h}{N_h} \tag{28}$$

  Through (27), at the beginning of the prediction only the measurement is considered, while progressively increasing significance is given to the preview-based lateral acceleration, $a_{y,prev} = r_{ref}(k_h)V_{est}$, along the prediction.

4.5. Auxiliary control blocks

The VSM vehicle model for control system assessment as well as the prediction model of NMPC-8 include the longitudinal vehicle dynamics, which are – instead – neglected by the OFLQR model for control design and the NMPC-3 prediction model. Therefore, a dedicated torque distribution block, used only by OFLQR and NMPC-3, see Figure 1, computes the individual wheel torque levels as:

$$T_{ij} = \frac{T_{dem}}{4} + \frac{M_{z,ext}R_{w,l}}{2b_i}[-1]^{\eta} \tag{29}$$

where the index η, with $\eta = 1, 2$, indicates the left or right vehicle sides. The wheel slip control function for traction and braking is embedded in NMPC-8 through (x) and (xiii) in

(18), while is omitted in OFLQR and NMPC-3, where it should be implemented at the corner level with possible feedback towards the direct yaw moment computation layer, see the recent analysis on centralised and multi-layer TV architectures including wheel slip control in [42]. Given the focus on manoeuvres without significant longitudinal accelerations, the simplification does not have any impact on the results of this study.

The suspension force distribution function calculates the reference active contributions of the actuator forces, according to:

$$F_{act,Fj} = \frac{k m_s a_y d f_{roll}}{b_F IR_F}[-1]^{\eta} \tag{30}$$

$$F_{act,Rj} = \frac{k m_s a_y d[1 - f_{roll}]}{b_R IR_R}[-1]^{\eta} \tag{31}$$

where IR_i is the installation ratio of the suspension actuators of the respective axle.

The brake blending block outputs the motor torque values during regeneration through $T_{em,ij} = \max(T_{ij}, T_{em,min,ij})$.

The controller operation requires the measurements from an inertial measurement unit, and, for NMPC-8, from wheel speed sensors. For simplicity, the simulation architecture does not include any estimation system, as this topic is not the focus of the analysis. Nevertheless, the estimation requirements for NMPC-3 and NMPC-8 are aligned with those of conventional vehicle stability controllers, requiring the slip ratio, slip angle, and approximate tyre-road friction level at each corner, and do not imply any specific criticality. The roll angle and roll rate, which must be provided to NMPC-3 and NMPC-8 as initial conditions for the prediction, can be obtained from the vehicle system kinematics and the measurements of suspension actuator displacements and body roll rate, carried out by the dedicated actuator sensors and the inertial measurement unit, according to a set-up already validated by Tenneco.

4.6. Controller implementation

All controllers were set up in the framework in Figure 1(c). OFLQR was run at a time step of 20 ms. NMPC-3 and NMPC-8 were implemented through the ACADO toolkit [28, 29], with the following settings: Gauss Newton Hessian approximation, multiple shooting discretisation, fourth order implicit Runge Kutta integrator, and qpOASES solver. Unless otherwise specified, in the remainder the NMPCs have $N_h = 2$ and $T_s = 35$ ms, corresponding to a 70 ms prediction horizon. The discretisation time of the internal model is 1 ms, ensuring numerical stability without significantly affecting computational time. With such settings, both NMPC-3 and NMPC-8 are real-time capable on a dSPACE MicroAutoBox II system (900 MHz, 16 Mb flash memory). Nevertheless, more computationally demanding settings can be explored, as more powerful hardware is currently available, and further progress is expected in the near future.

5. Simulation results

5.1. Test scenarios and performance indicators

The simulation results focus on limit handling conditions, represented by the following manoeuvres:

- Multiple step steer, consisting of a first step steering input on the left, with a 110 deg magnitude and a rate of 500 deg/s, followed, after ~ 2 s, by a step steering input to the right, with the same rate, to reach -110 deg, and finally, after further ~ 2 s, by a step steering input to the final condition $\delta_{sw} = 0$ deg. The manoeuvre is carried out from an initial speed of 120 km/h, with $\theta_{acc} = 20\%$.
- Sinusoidal steering, based on experimental inputs applied by a professional test driver, with an approximately sinusoidal δ_{sw} profile with an amplitude of ~ 160 deg at ~ 0.8 Hz, which tends to excite the yaw rate resonance, from an initial speed of 100 km/h, with $\theta_{acc} = 20\%$.

Unless otherwise specified, the manoeuvres are performed in high tyre-road friction conditions. Given the focus on limit handling, the considered key performance indicators (KPIs) are based on the yaw rate and sideslip angle response:

- The root mean square (RMS) value of the error between the reference and actual yaw rates, Δr_{RMS}, which evaluates the yaw rate tracking performance.
- The RMS value of sideslip angle, β_{RMS}, which evaluates the overall sideslip level.
- The maximum sideslip angle magnitude, $|\beta|_{max}$, which assesses the level of vehicle stability criticality.

The analyses with the VSM model from Section 2 cover the following EV configurations: (a) Passive, i.e. the EV without TV nor active suspension; (b) OFLQR; (c) NMPC-3 (Offline), i.e. NMPC-3 with the offline method for computing the lateral axle force formulation parameters, see Section 3.2; (d) NMPC-3 (Online), i.e. NMPC-3 coupled with the online method for obtaining the force parameters; (e) NMPC-8; (f) NMPC-3-Pre, i.e. the preview version of NMPC-3; and (g) NMPC-8-Pre, i.e. NMPC-8 with preview. Since a similar version of NMPC-8 without preview has been contrasted in [10] with a PI-based algorithm for anti-roll moment distribution and TV, the reader can refer to that study for a comparison with a baseline controller, and NMPC-8 can be considered the benchmark here.

Unless otherwise specified, the cost function weights were tuned to minimise Δr_{RMS} without provoking undesired control action oscillations during the multiple step steer, through a brute force algorithm assessing performance for a grid of weights.

5.2. Effect the NMPC-3 parametrisation

The yaw rate response along the manoeuvres is reported in Figure 4 for NMPC-3 (Online) and NMPC-3 (Offline), while the KPIs are in Table 2. The online method brings an improvement, visible in the majority of the sections of the manoeuvres, with reduced

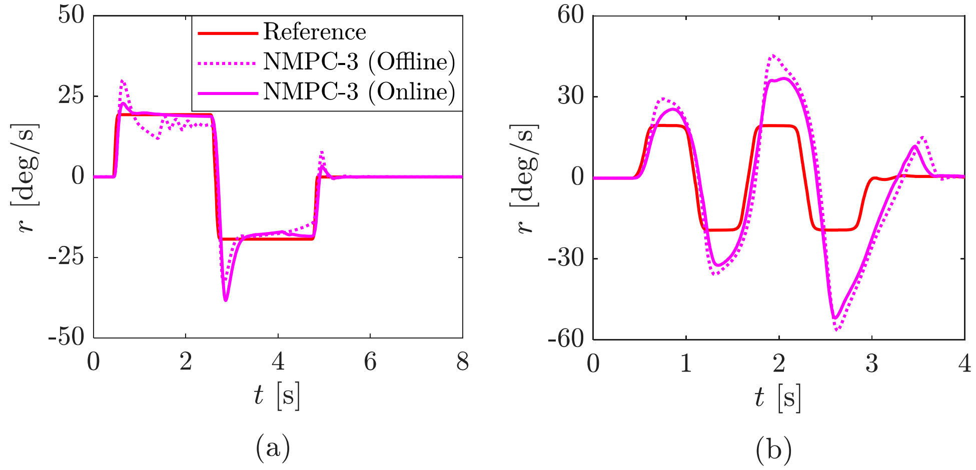

Figure 4. Yaw rate tracking performance of NMPC-3 (Online) and NMPC-3 (Offline) during: (a) the sequence of step steers; and (b) the sinusoidal steering test (only one reference is reported as it is the same for the two controllers).

Table 2. Performance indicators for the considered controllers during the two manoeuvres in nominal conditions.

	Multiple step steer test			Sinusoidal steering test		
Controller	Δr_{RMS} [deg/s]	β_{RMS} [deg]	$\|\beta\|_{max}$ [deg]	Δr_{RMS} [deg/s]	β_{RMS} [deg]	$\|\beta\|_{max}$ [deg]
Passive	7.63	9.39	27.49	7.33	3.37	18.32
OFLQR	2.54	1.93	4.88	5.53	1.57	8.32
NMPC-3 (Offline)	2.50	1.25	3.24	6.28	1.77	8.68
NMPC-3 (Online)	2.39	1.64	4.04	5.22	1.48	7.89
NMPC-8	2.11	1.35	3.14	2.33	0.47	2.17

yaw rate peaks, and a decrease of Δr_{RMS}, amounting to 2.39 and 5.22 deg/s for NMPC-3 (Online) along the multiple step steer and sinusoidal steering test, and to 2.50 and 6.28 deg/s for the offline method.

In the first test, in which, after the first steering input, $|r_{ref}|$ is higher than the yaw rate magnitude of the passive vehicle, the online parametrisation allows reaching the correct steady-state yaw rate between 0.5 and 2.3 s, which, given the sport-oriented nature of the reference, implies increased $|\beta|$ for NMPC-3 (Online). In fact, β_{RMS} is 1.64 and 1.25 deg, while $|\beta|_{max}$ is 4.04 and 3.24 deg, for NMPC-3 (Online) and NMPC-3 (Offline). On the contrary, in the second test, in which the dynamics and overshoots are more critical, NMPC-3 (Online) reduces both β_{RMS} (from 1.77 deg to 1.48 deg) and $|\beta|_{max}$ (from 8.68 deg to 7.89 deg, such large values are caused by the selected sport-oriented tuning of r_{ref}).

The conclusion is that the better yaw rate tracking of the online parameter estimation set-up makes the vehicle more agile in proximity of the cornering limit, and more stable when it operates beyond the limit of handling, which is very desirable. For these reasons, NMPC-3 (Online) is selected for the following analyses, and will be simply referred to as NMPC-3.

5.3. Comparison of OFLQR, NMPC-3, and NMPC-8

The profiles of the main variables for all cases along the two manoeuvres are in Figures 5 and 6. The KPIs are in Table 2, while Figure 7 reports the KPI percentage reduction, i.e. the improvement of the controlled cases w.r.t. the passive configuration.

The passive vehicle struggles coping with the extreme conditions of both tests, which results in $|\beta|_{max}$ exceeding 25 and 15 deg. While in the first test the passive case still follows the steering profile with a corresponding shape of the yaw rate response, although characterised by significant delays and overshoots, in the second half of the sinusoidal steering manoeuvre the profiles of a_y, r and φ do not follow the driver input any longer, i.e. the cornering direction reversal does not occur.

On the contrary, all controllers generate profiles of the variables that are consistent with the steering inputs. NMPC-8 achieves the highest improvement for all indicators, with 72% and 68% Δr_{RMS} reductions compared to the passive case for the two tests, which is followed by NMPC-3 with 68% and 29%, and OFLQR with 67% and 25%. More importantly, NMPC-8 excels in reducing the yaw rate overshoots w.r.t. the reference; for example, after the steering angle reversal in the sinusoidal steering test, the peak of r_{ref} is -19 deg/s, while r reaches -26 deg/s for NMPC-8, -32 deg/s for NMPC-3, -34 deg/s for OFLQR, and -64 deg/s for the passive configuration. NMPC-8 also manages to compensate any sideslip angle overshoot following the fast steering inputs, see the major reduction of $|\beta|_{max}$, which is less than one third than for the other controller configurations in the sinusoidal steering test. The difference is amplified by the sport-oriented tuning of r_{ref}, i.e. a more understeering reference behaviour would have limited the overshoots also for NMPC-3 and OFLQR. Nevertheless, Figures 5–7 show that NMPC-8 can generate handling behaviour that is simultaneously very responsive and safe.

The control inputs highlight a more aggressive behaviour of NMPC-8, e.g. see the wheel torque profiles in Figure 6, which increases effectiveness. It was verified that a similar behaviour would not have been achievable with a different tuning of NMPC-3, for which an increase of the yaw rate tracking weight would have provoked undesired oscillations of the cornering response.

In conclusion, the consideration of the nonlinear tyre behaviour of NMPC-8, and the complexity and accuracy of its internal model bring performance benefits. However, these are associated with a computational effort penalty. In fact, although all configurations operate in real time on the same rapid control prototyping unit, in the considered conditions the maximum turnaround time is $\sim 2 \cdot 10^{-5}$ s for OFLQR, ~ 2 ms for NMPC-3, and ~ 33 ms for NMPC-8.

Despite not being considered explicitly in the proposed NMPC formulations, the inherent robustness and stability of model predictive control have been widely discussed [43].

To assess robustness, the multiple step steer is repeated in Figure 8(a) for a tyre-road friction factor $\mu_{ij,0} = 0.6$, which is imposed in the VSM model, but is not provided to the controllers, i.e. the reference yaw rate and tyre forces in the prediction models assume $\mu_{ij,0} = 1.0$. This condition is far more critical than what could be expected from a current-generation estimator for vehicle dynamics applications. All controlled configurations tend to better track r_{ref} than the passive vehicle. However, in these extreme conditions, the soft constraint on $|\alpha_R|$ of NMPC-3 and NMPC-8 is vital to limit the $|\alpha_R|$ peaks to values marginally above 5 deg, which is not the case for OFLQR, having the only target of

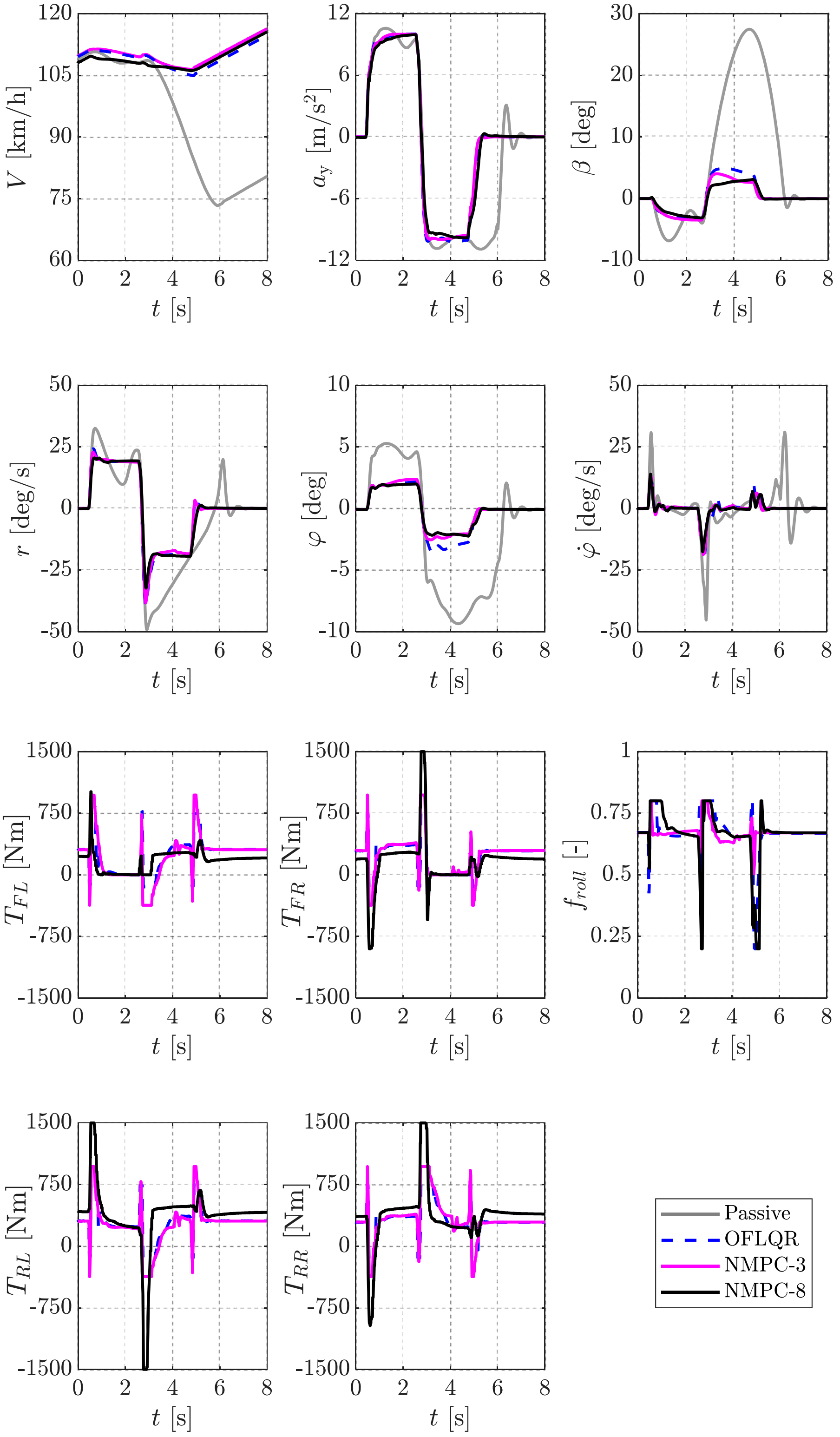

Figure 5. Comparison of vehicle states and control inputs for the considered vehicle configurations along the multiple step steer.

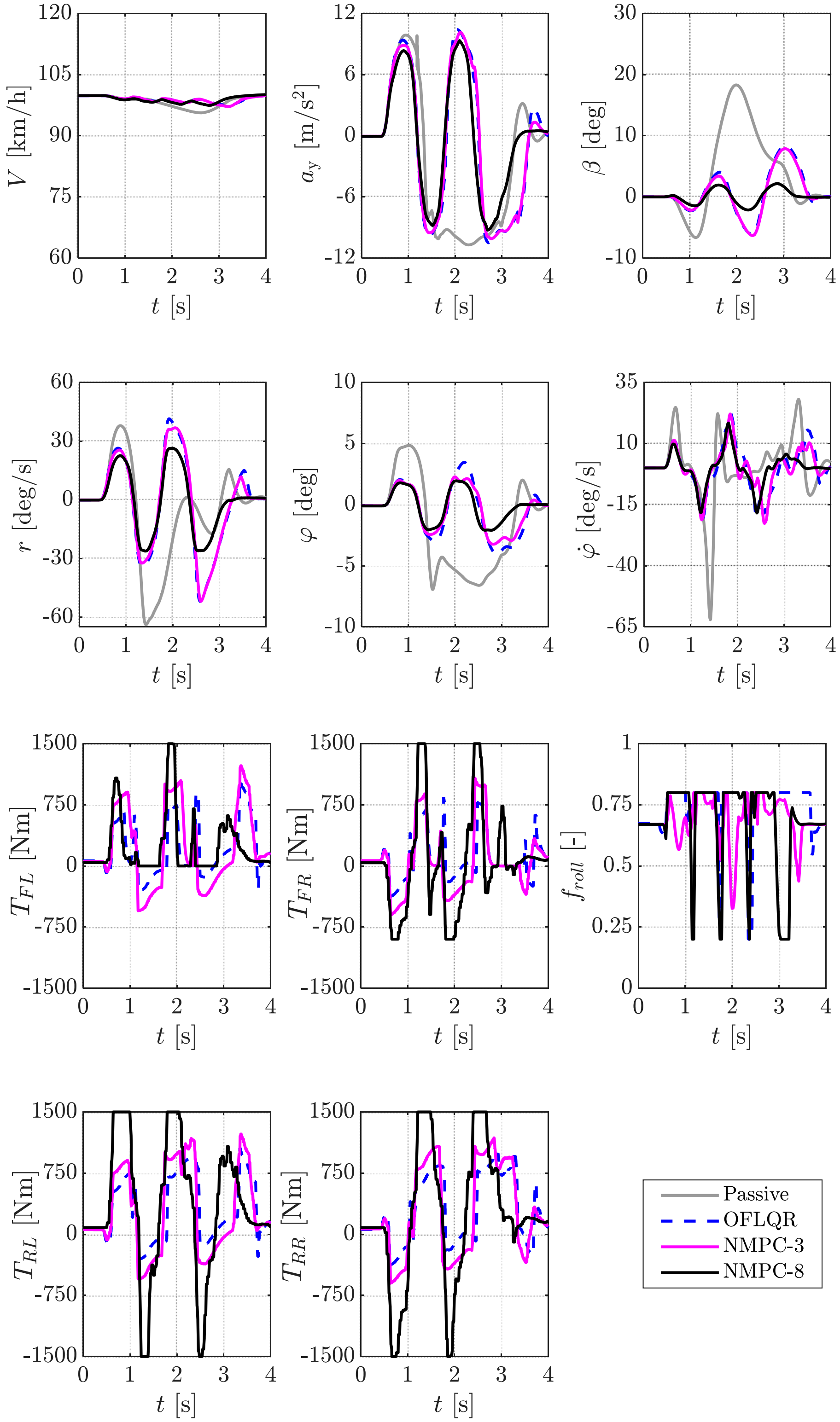

Figure 6. Comparison of vehicle states and control inputs for the considered vehicle configurations along the sinusoidal steering manoeuvre.

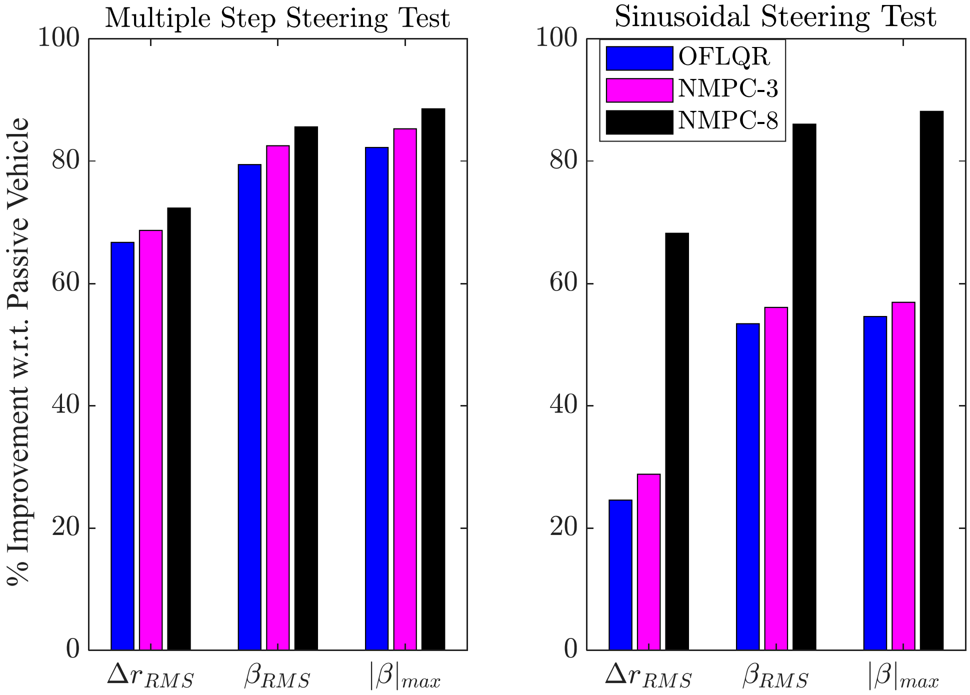

Figure 7. KPI reduction for the three controllers w.r.t. the passive vehicle.

tracking r_{ref}. The rear slip angle constraint of the NMPCs brings a corresponding reduction of $|r|$, especially after the second steering input, which is the most critical one, as it is associated with a change of sign of the lateral load transfers. In the same section of the manoeuvre, differently from NMPC-3, NMPC-8 also compensates the yaw rate overshoot resulting from the steering transient, and confirms itself as the best controller.

The robustness assessment also includes the sensitivity to the independent variation of vehicle mass, m, and yaw mass moment of inertia, I_z, in the VSM model, in the [−20%, 20%] range during the multiple step steer test in high tyre-road friction, while the prediction models and controller calibrations are not varied. The top plots in Figure 8(b) show the resulting percentage reduction, $\Delta r_{RMS,red}$, of Δr_{RMS} w.r.t. the passive case, while the bottom plots report Δr_{RMS}. Across the considered realistic parameter space, $\Delta r_{RMS,red}$ exceeds 45% for NMPC-8, 36% for NMPC-3, and 27% for OFLQR, and the respective maximum Δr_{RMS} values are 3.54, 4.27, and 4.83 deg/s.

For completeness, a Monte Carlo stability analysis is carried out along the multiple step steer. The simulations cover test scenarios for a combination of parameter values randomly drawn from the respective normal probability distribution, see Figure 9. The considered parameters are: (i) Δm; (ii) ΔI_z; (iii) W_{C_y}, i.e. the scaling factor on the cornering stiffness in the Pacejka model; (iv) W_{K_y}, the scaling factor on lateral stiffness of the tyre sidewalls, which is inversely proportional to the relaxation length; (v) $\mu_{ij,0}$; and (vi) $V_{initial}$, i.e. the initial vehicle speed of the manoeuvre. (i)–(v) are varied only in the high-fidelity VSM model, while they are not changed in the prediction models, and do not have any impact on the OFLQR. On the contrary, (vi) is provided also to the controllers, as it would be output by

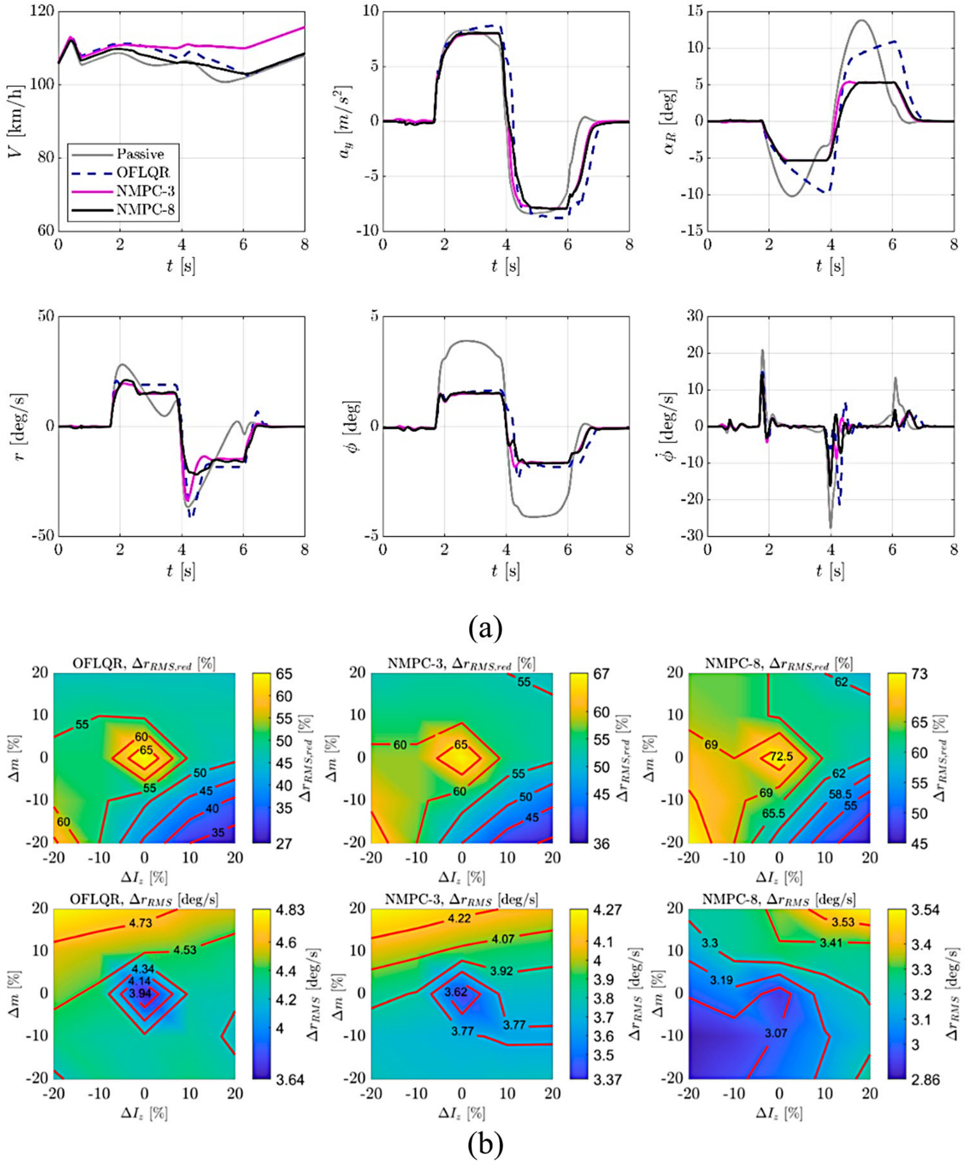

Figure 8. Robustness analyses: (a) Comparison of the main vehicle variables for the considered vehicle configurations along the multiple step steer manoeuvre, with $\mu_{ij,0}$ =0.6 imposed only in the VSM model; and (b) Carpet plots of $\Delta r_{RMS,red}$ and Δr_{RMS} for the considered vehicle configurations along the multiple step steer manoeuvre, as a function of percentage variations of vehicle mass and yaw mass moment of inertia, Δm and ΔI_z.

the on-board state estimator. The results reported in Table 3 show that ∼2% of the simulations of the passive vehicle imply unstable behaviour, i.e. the vehicle spins after the second steering input, while in 46% of the runs, although being stable, the passive response is characterised by $|\alpha_R|$ peaks (i.e. $|\alpha_R|_{max}$) exceeding 20 deg. OFLQR, NMPC-3, and NMPC-8 prevent spinning and reduce $|\alpha_R|_{max}$ in all cases, which confirms the robustness of the

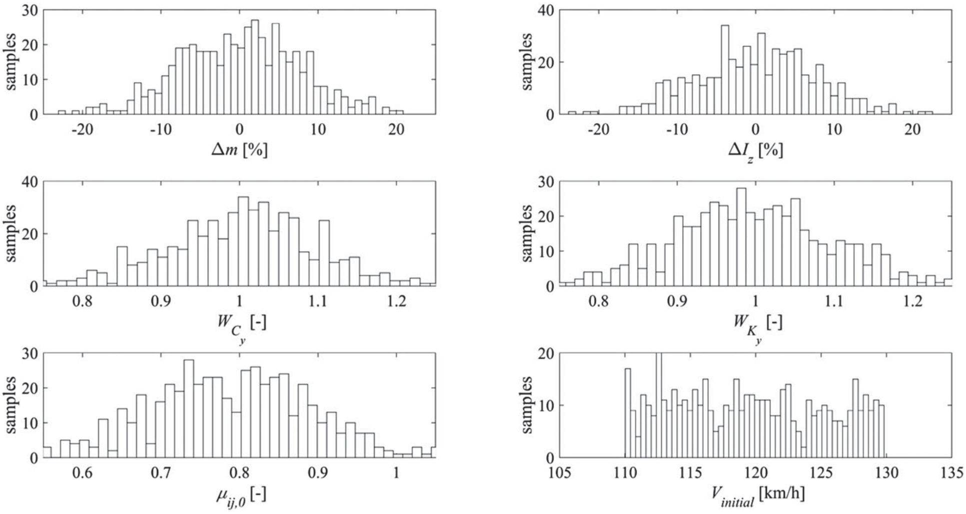

Figure 9. Robustness analyses: parameter values distribution for the Monte Carlo simulations during the multiple step steer.

Table 3. Results of the Monte Carlo analysis for the passive, OFLQR, NMPC-3, and NMPC-8 configurations.

Controller	Simulation runs [%] with unstable behaviour	Simulation runs [%] with $\lvert\alpha_R\rvert_{max} > 20$ deg	Average value of $\lvert\alpha_R\rvert_{max}$ [deg]
Passive	~ 2%	~ 46%	17.9
OFLQR	0%	~ 14%	13.4
NMPC-3	0%	~ 14%	11.6
NMPC-8	0%	~ 2%	6.0

implementations. More specifically, $|\alpha_R|_{max}$ exceeds 20 deg in 14% of the simulations for OFLQR and NMPC-3, and in only 2% of the runs for NMPC-8, which manages to keep the rear slip angle peak within ~ 5 deg in 80% of the tests. For the parametrisations in which the passive vehicle does not spin, the average value of $|\alpha_R|_{max}$ amounts to 17.9, 13.4, 11.6, and 6.0 deg, respectively for the passive, OFLQR, NMPC-3, and NMPC-8 configurations.

5.4. Effect of preview

5.4.1. Effect of preview on NMPC-3

For the sinusoidal steering test, Figure 10 reports r_{ref} and r for NMPC-3 and NMPC-3-Pre for: (i) $N_h = 2$ and $T_s = 35$ ms, corresponding to $t_h = 70$ ms; and (ii) $N_h = 10$ and $T_s = 50$ ms, corresponding to $t_h = 500$ ms. All configurations use the same cost function weight calibrations as in Section 5.3. While in (i) the preview brings marginally improved yaw rate tracking, in (ii) it corresponds to significantly higher yaw rate oscillations. In fact, while the preview is expected to increase performance with increasing t_h when associated with NMPCs embedding realistic prediction models, the linearisation of the lateral axle force of the NMPC-3 prediction model can cause significant inaccuracies, and thus a controller

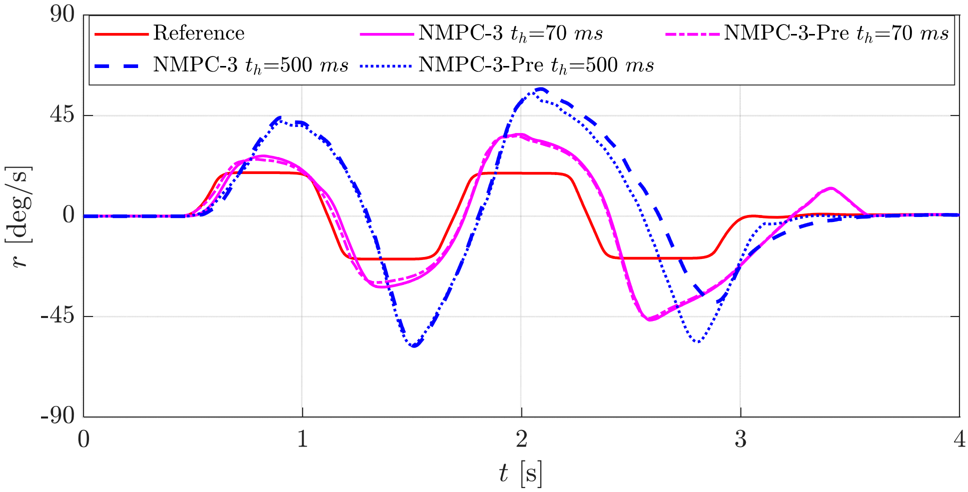

Figure 10. Yaw rate tracking performance of NMPC-3 and NMPC-3-Pre with $t_h = 70$ ms ($N_h = 2$ and $T_s = 35$ ms) and $t_h = 500$ ms ($N_h = 10$ and $T_s = 50$ ms), along the sinusoidal steering test.

performance decay, for longer t_h. As extensive simulations confirmed that this is a general trend for NMPC-3, the following analyses are limited to NMPC-8.

5.4.2. NMPC-8-Pre performance with different prediction settings

Since the preliminary assessment of the preview strategy showed substantially aligned performance for NMPC-8-Pre using constant lateral acceleration along t_h, or variable a_y according to (27) and (28), the following results refer to the first option.

Figure 11 compares the yaw rate profiles for NMPC-8 and NMPC-8-Pre for combinations of N_h and T_s along the sinusoidal steering test, while keeping the cost function weights equal to their original optimal (baseline, BL) calibration for $N_h = 2$ and $T_s = 35$ ms. Subplots (a) and (b) of Figure 12 highlight the KPI percentage reduction of NMPC-8 and NMPC-8-Pre w.r.t. the passive configuration, while subplot (c) reports the KPI percentage reduction of NMPC-8-Pre w.r.t. to the corresponding NMPC-8 with the same prediction settings.

The NMPC-8 performance does not improve with longer t_h, and its best Δr_{RMS} results are for $N_h = 2$ and $T_s = 50$ ms (73% Δr_{RMS} reduction w.r.t. the passive case) and $N_h = 2$ and $T_s = 20$ ms, indicated as '1' and '2' in Figure 12(a). On the contrary, NMPC-8-Pre achieves its best performance for longer t_h, corresponding to $N_h = 10$ and $T_s = 50$ ms (79% Δr_{RMS} reduction) and $N_h = 15$ and $T_s = 50$ ms, see '1' and '2' in Figure 12(b). NMPC-8-Pre is consistently effective across the settings, and always brings KPI reductions exceeding 60% w.r.t. the passive configuration, as opposed to NMPC-8, whose performance significantly varies with the prediction parameters, with a deterioration for $N_h \geq 10$ and $T_s = 50$ ms, which indicates the need for weight recalibration. For all settings, NMPC-8-Pre outperforms NMPC-8 in terms of Δr_{RMS}, with reductions ranging from $\sim$5% for short horizons, to $\sim$71% for the longest t_h.

For completeness, the NMPC-8 cost function weights were re-calibrated through the brute force Δr_{RMS}-based method, for each of the prediction settings indicated with '1' and

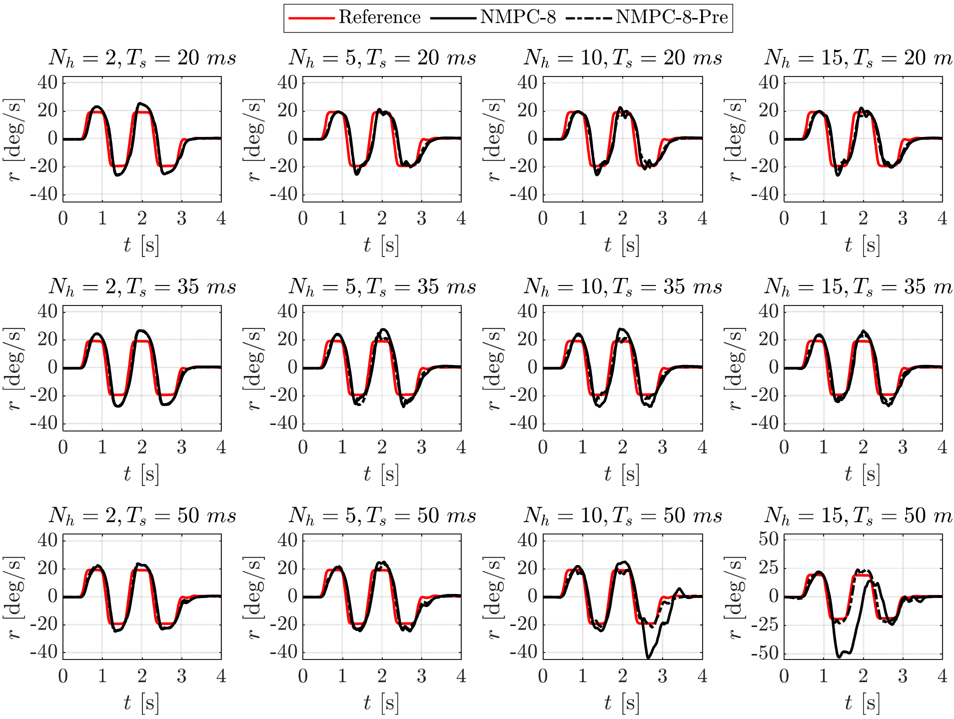

Figure 11. Comparison of the yaw rate tracking performance of NMPC-8 and NMPC-8-Pre along the sinusoidal steering test.

‘2’ in Figure 12(a,b), for a total of four optimised configurations. The same weights were also applied to the NMPC-8-Pre version operating with the corresponding setting, to guarantee conservativeness in the assessment, i.e. the comparison was carried out for weights that were optimised for NMPC-8. The resulting KPI variations of each controller in its initial baseline calibration (indicated as ‘BL tuning’) and re-tuned configuration, w.r.t the passive configuration, are in Figure 13(a,b). The sensitivity to weight calibration is more evident for NMPC-8, which, after re-tuning, manages to achieve good performance for all prediction settings, including those with long t_h, although the results are always inferior to those of the corresponding preview configurations. After calibration, the relative ranking of the controllers in terms of Δr_{RMS} does not change, i.e. settings 1 of NMPC-8 and NMPC-8-Pre still achieve better yaw rate tracking than the respective settings 2.

As a summary, Figure 13(c) plots the KPI improvement of the baseline and re-tuned configurations of setting 1 of NMPC-8-Pre, w.r.t. the corresponding setting 1 of the baseline and re-tuned NMPC-8. The preview benefit is evident, with reductions of Δr_{RMS} by 23% and 19%, β_{RMS} by 28% and 24%, and $|\beta|_{max}$ by 10% and 37%, respectively with the baseline tuning and after the NMPC-8-oriented recalibration. These results, together with the significantly higher robustness of NMPC-8-Pre w.r.t. the variation of the cost function weights, make preview-based control a relevant and competitive option to be further explored for next generation ICCs.

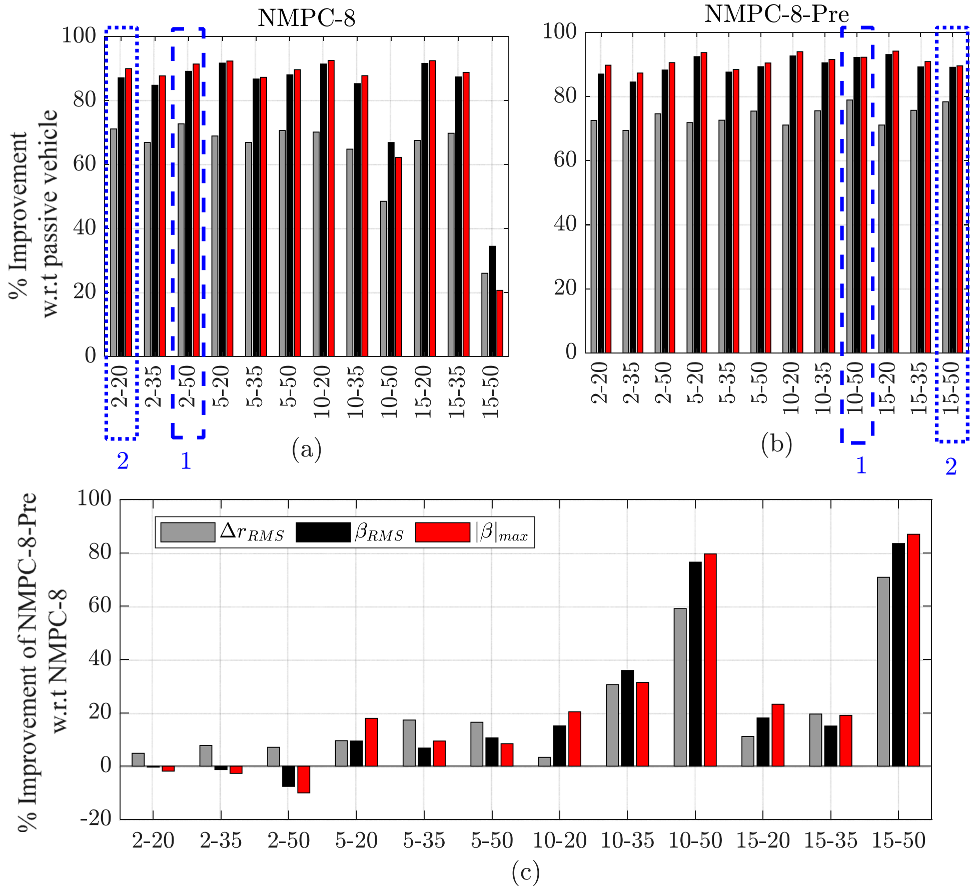

Figure 12. Sinusoidal steering test: (a) KPI reduction of NMPC-8 w.r.t. passive; (b) KPI reduction of NMPC-8-Pre w.r.t. passive; and (c) KPI reduction of NMPC-8-Pre w.r.t. NMPC-8, for different prediction horizon settings, indicated by the values of N_h and T_s (in ms) at the bottom of each histogram. The notations '1' and '2' refer to the two settings providing the lowest Δr_{RMS} for NMPC-8 (subplot (a)) and NMPC-8-Pre (subplot (b)).

5.4.3. *Effect of steering angle prediction error on NMPC-8-Pre*

A sensitivity analysis was conducted to investigate the effect of the steering angle prediction error. Instead of feeding NMPC-8-Pre with the correct discretised $\delta_{sw}(k_h)$ profile, a modified steering profile prediction, $\delta_{sw,mod}(k_h)$, is used, according to:

$$\delta_{sw,mod}(k_h) = [1 + C_f(k_h)]\delta_{sw}(k_h) \tag{32}$$

where $C_f(k_h)$ is the non-dimensional prediction error. In the initial part the prediction horizon, the error is likely to be small, as the prediction is going to be based on a minor deviation w.r.t. the measured δ_{sw} value, while the deviation is likely to increase with increasing k_h. Therefore, $C_f(k_h)$ is linearly varied from 0 at the beginning of the prediction, to $C_{f,max}$ at t_h, according to $C_f(k_h) = C_{f,max}k_h/N_h$. The reference yaw rate prediction is computed by feeding $\delta_{sw,mod}(k_h)$ into the r_{ref} map.

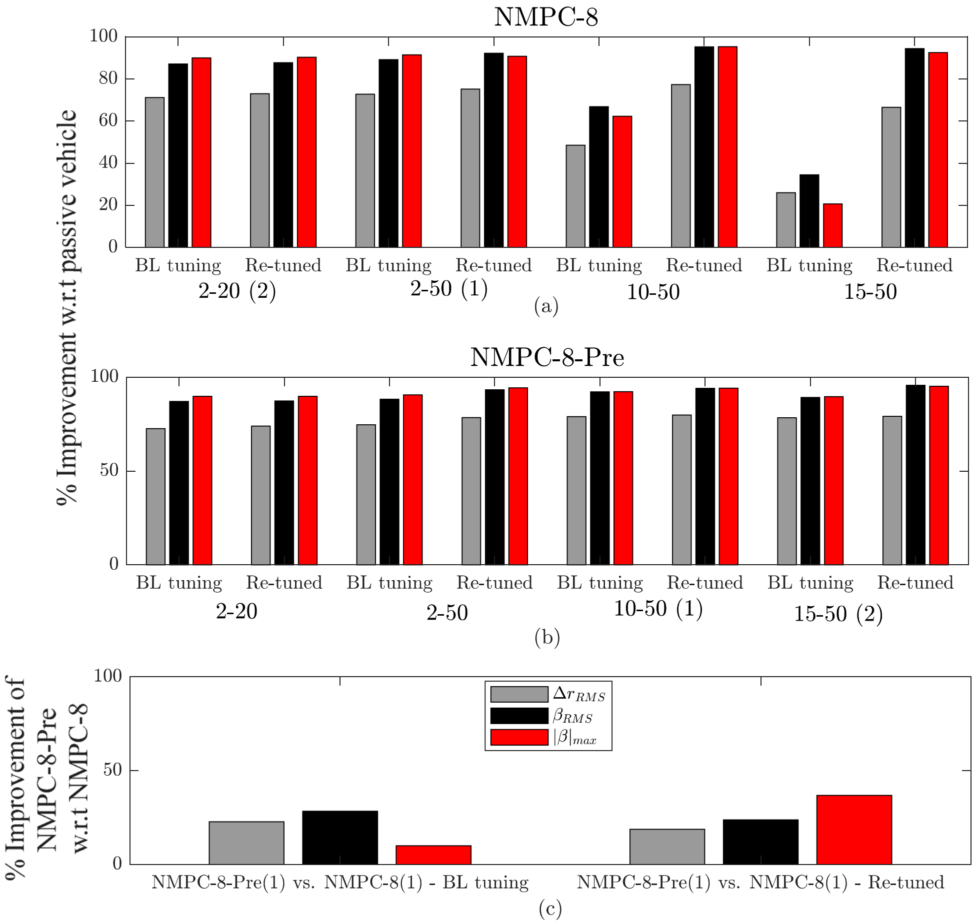

Figure 13. Sinusoidal steering test: comparisons of the baseline (BL) tuning and re-tuned calibrations of NMPC-8 and NMPC-8-Pre, for settings 1 and 2 in Figure 12. (a) KPI reduction of NMPC-8 w.r.t. passive; (b) KPI reduction of NMPC-8-Pre w.r.t. passive; and (c) KPI reduction of NMPC-8-Pre (setting 1) w.r.t. NMPC-8 (setting 1).

The yaw rate tracking results are in Figure 14, which compares NMPC-8 (receiving the correct steering input at the current time) with NMPC-8-Pre for $C_{f,max}$ =0, 0.5 and 1, where $C_{f,max} = 0$ denotes the preview controller with ideal steering predictions. Interestingly, in the specific test, NMPC-8-Pre is able to tolerate up to 100% error in terms of steering input amplitude, and the corresponding reference yaw rate error, and to still improve yaw rate tracking, which confirms the real-world potential of the proof-of-concept implementations. For the simulations in Figure 14(a), Δr_{RMS} is 2.43 deg/s for NMPC-8, and 2.24, 2.34 and 2.39 deg/s for NMPC-8-Pre respectively with $C_{f,max}$ =0, 0.5 and 1, while in Figure 14(b) Δr_{RMS} is 1.82 deg/s for NMPC-8, and < 1.50 deg/s for all the NMPC-8-Pre cases.

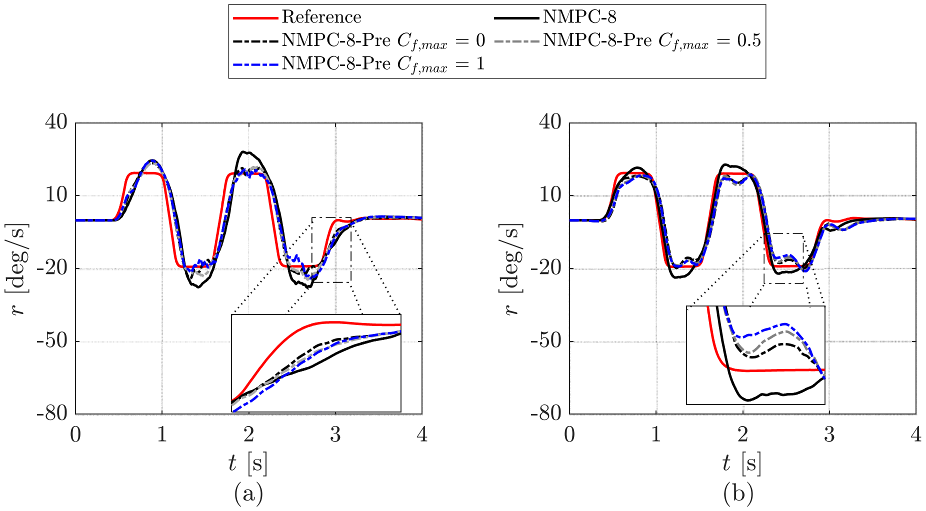

Figure 14. Yaw rate tracking performance along the sinusoidal steering test for: (a) the BL tunings of NMPC-8 and NMPC-8-Pre, for $N_h = 2$ and $T_s = 35$ ms; and (b) the re-tuned versions of settings 1 of NMPC-8 ($N_h = 2$ and $T_s = 50$ ms) and NMPC-8-Pre ($N_h = 10$ and $T_s = 50$ ms). For NMPC-8-Pre the cases with $C_{f,max} = 0$, 0.5 and 1 are considered.

6. Conclusions

This study analysed three formulations for integrated direct yaw moment and anti-roll moment distribution control, for an electric vehicle with in-wheel motors, brake-by-wire, and active suspensions. The controllers are an output feedback linear quadratic regulator (OFLQR), and two nonlinear model predictive formulations, using 3- and 8-DoF prediction models, and neglecting (this is the case of NMPC-3 and NMPC-8) or considering (NMPC-3-Pre and NMPC-8-Pre) the future profiles of steering angle and reference yaw rate, in the context of preview-based control of connected vehicles.

The simulations of transient manoeuvres in limit handling conditions with an experimentally validated model bring the following conclusions:

- NMPC-8 outperforms NMPC-3 and OFLQR in terms of yaw rate tracking, see the reductions of the root mean square values of the yaw rate error, Δr_{RMS}, and also compensates the sideslip angle overshoots following fast steering inputs, see the maximum sideslip angle magnitude, $|\beta|_{max}$, which is reduced by a factor 3 in the sinusoidal steering test. The superior performance of NMPC-8 is also confirmed by the robustness analysis with respect to independent variations of vehicles mass and yaw mass moment of inertia. Such benefits justify the computational load of NMPC-8.
- For low tyre-road friction manoeuvres, the soft constraint on $|\alpha_R|$ of NMPC-3 and NMPC-8 is vital to limit the $|\alpha_R|$ peaks to values marginally above 5 deg, which is not the case for OFLQR, having the only target of tracking r_{ref}.
- All formulations without preview run in real-time on the same rapid control prototyping unit, with maximum turnaround times of $\sim 2{\cdot}10^{-5}$ s for OFLQR, ~ 2 ms for NMPC-3, and ~ 33 ms for NMPC-8, along the considered manoeuvres.

- As NMPC-3-Pre, although being nonlinear, uses a linearised lateral axle force formulation, the effect of preview, which should favour relatively long prediction horizons, becomes counterproductive if the internal model covers predictions that extend to conditions that are far from the original linearisation point.
- The performance of NMPC-8-Pre systematically exceeds the one of the corresponding NMPC-8. For example, when comparing the best performing configurations of the two cases, the preview implementation brings reductions of Δr_{RMS} by 19%, β_{RMS} (root mean square value of the sideslip angle) by 24%, and $|\beta|_{max}$ by 37%, during the sinusoidal steering test. Moreover, NMPC-8-Pre, differently from NMPC-8, is robust w.r.t. the calibration of the cost function weights.
- In the selected manoeuvres, the NMPC-8-Pre benefit over NMPC-8 persists also for significant errors on the steering angle and reference yaw rate profiles along the prediction horizon.

Disclosure statement

No potential conflict of interest was reported by the author(s).

Funding

This work was supported by the Horizon 2020 Programme of the European Commission under grant agreement no. 824250 (EVC1000 project).

ORCID

M. Dalboni http://orcid.org/0000-0002-3890-4254
P. Gruber http://orcid.org/0000-0003-1030-6655
A. Sorniotti http://orcid.org/0000-0002-4848-058X

References

[1] Tavernini D, Metzler M, Gruber P, et al. Explicit nonlinear model predictive control for electric vehicle traction control. IEEE Trans Control Syst Technol. 2019;27(4):1438–1451. doi:10.1109/TCST.2018.2837097.

[2] Zhou H, Jia F, Jing H, et al. Coordinated longitudinal and lateral motion control for four wheel independent motor-drive electric vehicle. IEEE Trans Veh Technol. 2018;67(5):3782–3790. doi:10.1109/TVT.2018.2816936.

[3] Sawamura D, Fujimoto H. Minimum collision avoidance distance control for four-wheel-driven electric vehicles with active front and rear steerings. IEEE Int Conf Mech (ICM). 2015: 341–346.

[4] Wang Y, Gao J, Li K, et al. Integrated design of control allocation and triple-step control for over-actuated electricdian ground vehicles with actuator faults. J Franklin Inst. 2020;357(6):3150–3167. doi:10.1016/j.jfranklin.2019.07.035.

[5] De Novellis L, Sorniotti A, Gruber P, et al. Direct yaw moment control actuated through electric drivetrains and friction brakes: theoretical design and experimental assessment. Mechatronics. 2015;26:1–15. doi:10.1016/j.mechatronics.2014.12.003.

[6] Zhang L, Ding H, Huang Y, et al. An analytical approach to improve vehicle maneuverability via torque vectoring control: theoretical study and experimental validation. IEEE Trans Veh Technol. 2019;68(5):4514–4526. doi:10.1109/TVT.2019.2903872.

[7] Siampis E, Velenis E, Longo S. Rear wheel torque vectoring model predictive control with velocity regulation for electric vehicles. Veh Syst Dyn. 2015;53(11):1555–1579. doi:10.1080/00423114.2015.1064972.

[8] De Filippis G, Lenzo B, Sorniotti A, et al. Energy-efficient torque-vectoring control of electric vehicles with multiple drivetrains. IEEE Trans Veh Technol. 2018;67(6):4702–4715. doi:10.1109/TVT.2018.2808186.

[9] Chatzikomis C, Zanchetta M, Gruber P, et al. An energy-efficient torque-vectoring algorithm for electric vehicles with multiple motors. Mech Syst Signal Process. 2019;128:655–673. doi:10.1016/j.ymssp.2019.03.012.

[10] Dalboni M, Tavernini D, Montanaro U, et al. Nonlinear model predictive control for integrated energy-efficient torque-vectoring and anti-roll moment distribution. IEEE/ASME Trans Mechatron. 2021;26(3):1212–1224. doi:10.1109/TMECH.2021.3073476.

[11] Ueno K, Fujibayashi T, Sasaki M, et al. Vehicle control techniques for safety, environmental performance, and ride comfort. Hitachi Rev. 2018;67(1):64–71.

[12] Williams DE, Haddad WM. Nonlinear control of roll moment distribution to influence vehicle yaw characteristics. IEEE Trans Control Syst Technol. 1995;3(1):110–116. doi:10.1109/87.370716.

[13] Abe M. A study on effects of roll moment distribution control in active suspension on improvement of limit performance of vehicle handling. Int J Veh Des. 1994;15(3/4/5):326–336. doi:10.1504/IJVD.1994.061865.

[14] Cooper N, Crolla D, Levesley M. Integration of active suspension and active driveline to ensure stability while improving vehicle dynamics. *SAE Technical Paper 2005-01*-0414. 2005.

[15] Zhu Q, Ayalew B. Predictive roll, handling and ride control of vehicles via active suspensions. American Control Conference. 2014: 2102–2107.

[16] Ricco M, Zanchetta M, Rizzo GC, et al. On the design of yaw rate control via variable front-to-total anti-roll moment distribution. IEEE Trans Veh Technol. 2020;69(2):1388–1403. doi:10.1109/TVT.2019.2955902.

[17] Ricco M, Percolla A, Rizzo GC, et al. On the model-based design of front-to-total anti-roll moment distribution controllers for yaw rate tracking. Veh Syst Dyn. 2020;60(2):569–596. doi:10.1080/00423114.2020.1825753.

[18] Mazzilli V, De Pinto S, Pascali L, et al. Integrated chassis control: classification, analysis and future trends. Annu Rev Control. 2021;51:172–205. doi:10.1016/j.arcontrol.2021.01.005.

[19] Ahangarnejad AH, Melzi S, Ahmadian M. Integrated vehicle dynamics system through coordinating active aerodynamics control, active rear steering, torque vectoring and hydraulically interconnected suspension. Int J Auto Techn. 2019;20(5):903–915. doi:10.1007/s12239-019-0084-x.

[20] Ataei M, Khajepour A, Jeon S. Model predictive control for integrated lateral stability, traction/braking control, and rollover prevention of electric vehicles. Veh Syst Dyn. 2020;58(1):49–73. doi:10.1080/00423114.2019.1585557.

[21] Her H, Suh J, Yi K. Integrated control of the differential braking, the suspension damping force and the active roll moment for improvement in the agility and the stability. Proc Inst Mech Eng, Part D: J of Auto Eng. 2015;229(9):1145–1157. doi:10.1177/0954407014550502.

[22] Her H, Koh Y, Joa E, et al. An Integrated control of differential braking, front/rear traction, and active roll moment for limit handling performance. IEEE Trans Veh Technol. 2016;65(6):4288–4300. doi:10.1109/TVT.2015.2513063.

[23] Gerhard J, Laiou M-C, Monnigmann M, et al. Robust yaw control design with active differential and active roll control systems. IFAC Proc. 2005;38(1):73–78.

[24] Wang Q, Zhao Y, Lin F, et al. Integrated control for distributed in-wheel motor drive electric vehicle based on states estimation and nonlinear MPC. Proc Inst Mech Eng, Part D: J Auto Eng; 2022;236(5):893–906. doi:10.1177/09544070211030444.

[25] Chang S, Lee B, Park Y, et al. Integrated chassis control for improving on-center handling behaviour. SAE Int J Passenger Cars – Mech Syst. 2014;7(3):1002–1008. doi:10.4271/2014-01-0139.

[26] Adireddy G, Shim T. MPC based integrated chassis control to enhance vehicle handling considering roll stability. ASME Dyn Syst Cont Conf. 2011;2:877–884.

[27] Shim T, Margolis D. An analytical tire model for vehicle simulation in normal driving condition. Int J Veh Des. 2004;35(3):224–240. doi:10.1504/IJVD.2004.004950.

[28] Houska B, Ferreau HJ, Diehl M. ACADO toolkit—An open-source framework for automatic control and dynamic optimization. Opt Cont Appl Method. 2011;32(3):298–312. doi:10.1002/oca.939.

[29] Houska B, Ferreau HJ, Diehl M. An auto-generated real-time iteration algorithm for nonlinear MPC in the microsecond range. Automatica. 2011;47(10):2279–2285. doi:10.1016/j.automatica.2011.08.020.

[30] Parra A, Tavernini D, Gruber P, et al. On nonlinear model predictive control for energy-efficient torque-vectoring. IEEE Trans Veh Technol. 2021;70(1):173–188. doi:10.1109/TVT.2020.3022022.

[31] Yim S. Design of a preview controller for vehicle rollover prevention. IEEE Trans Veh Technol. 2011;60(9):4217–4226. doi:10.1109/TVT.2011.2169687.

[32] Yim S. Preview controller design for vehicle stability with V2V communication. IEEE Trans Intell Transp Syst. 2016;18(6):1497–1506. doi: 10.1109/TITS.2016.2607283.

[33] Parra A, Tavernini D, Gruber P, et al. On pre-emptive vehicle stability control. Veh Syst Dyn. 2022;60(6):2098–2123. doi:10.1080/00423114.2021.1895229.

[34] Armengaud E, Nager T, Gramstat S, et al. Electric wheel dual drive: functional integration for e-vehicle. In *International forum on advanced microsystems for automotive applications*. Berlin: Springer International; 2020. p. 211–222.

[35] Pacejka H. Tire and vehicle dynamics. Amsterdam: Elsevier; 2005.

[36] Genta G. Motor Vehicle dynamics: modeling and simulation. Singapore: World Scientific; 1997.

[37] Milliken WF, Milliken DL. Race car vehicle dynamics. Warrendale, PA: SAE International, 1994.

[38] Lu Q, Sorniotti A, Gruber P, et al. H_∞ loop shaping for the torque-vectoring control of electric vehicles: Theoretical design and experimental assessment. Mechatronics. 2016;35:32–43. doi:10.1016/j.mechatronics.2015.12.005.

[39] Mazzilli V, Ivone D, De Pinto S, et al. On the benefit of smart tyre technology on vehicle state estimation. Veh Syst Dyn. 2022;60(11):3694–3719. doi:10.1080/00423114.2021.1976414.

[40] Heidfeld H, Schünemann M, Kasper R. UKF-based State and tire slip estimation for a 4WD electric vehicle. Veh Syst Dyn. 2019;58(10):1–18. doi: 10.1080/00423114.2019.1648836.

[41] Ilka A. Matlab/Octave toolbox for structurable and robust output-feedback LQR design. IFAC-PapersOnLine. 2018;51(4):598–603. doi:10.1016/j.ifacol.2018.06.161.

[42] Rini G, De Bernardis M, Bottiglione F, et al. Comparison of centralized and multi-layer architectures for nonlinear model predictive torque-vectoring and traction control. Int J Auto Tech. 2023;24:1101–1116. doi:10.1007/s12239-023-0090-x.

[43] McAllister RD, Rawlings JB. Nonlinear stochastic model predictive control: existence, measurability, and stochastic asymptotic stability. IEEE Trans Autom Control. 2023;68(3):1524–1536. doi:10.1109/TAC.2022.3157131.

Appendix – Model for OFLQR design and NMPC-3 prediction

$$
\begin{aligned}
\dot{\beta} = -r + \frac{1}{mu}\Bigg\{ & F_{y,F,0} + F'_{y,F,0}\left\{\frac{u[\dot{\beta}+r][ma_R h_{roll}/l + m_s k f_{roll} d] + K_F\varphi + D_F\dot{\varphi}}{b_F} - \Delta F_{z,F,0}\right\} \\
& + \left\{C_{F,0} + C'_{F,0}\left\{\frac{u[\dot{\beta}+r][ma_R h_{roll}/l + m_s k f_{roll} d] + K_F\varphi + D_F\dot{\varphi}}{b_F} - \Delta F_{z,F,0}\right\}\right\} \\
& \times \left[\beta + \frac{a_F}{u} r - S - \alpha_{F,0}\right] \\
& + F_{y,R,0} + F'_{y,R,0}\left\{\frac{u[\dot{\beta}+r][ma_F h_{roll}/l + m_s k[1 - f_{roll}]d] + K_R\varphi + D_R\dot{\varphi}}{b_R} - \Delta F_{z,R,0}\right\} \\
& + \left\{C_{R,0} + C'_{R,0}\left\{\frac{u[\dot{\beta}+r][ma_F h_{roll}/l + m_s k[1 - f_{roll}]d] + K_R\varphi + D_R\dot{\varphi}}{b_R} - \Delta F_{z,R,0}\right\}\right\}
\end{aligned}
$$

$$\times\Bigg[\beta - \frac{a_R}{u} r - \alpha_{R,0}\Bigg]\Bigg\} \tag{A1}$$

$$\begin{aligned}
\dot{r} = \frac{1}{I_z} \Bigg\{ & M_{z,ext} + a_F \Bigg\{ F_{y,F,0} + F'_{y,F,0} \Bigg\{ \frac{u[\dot{\beta} + r][m a_R h_{roll}/l + m_s k f_{roll} d] + K_F \varphi + D_F \dot{\varphi}}{b_F} \\
& - \Delta F_{z,F,0} \Bigg\} \\
& + \Bigg\{ C_{F,0} + C'_{F,0} \Bigg\{ \frac{u[\dot{\beta} + r][m a_R h_{roll}/l + m_s k f_{roll} d] + K_F \varphi + D_F \dot{\varphi}}{b_F} - \Delta F_{z,F,0} \Bigg\}\Bigg\} \\
& \times \Bigg[\beta + \frac{a_F}{u} r - S - \alpha_{F,0}\Bigg]\Bigg\} \\
& - a_R \Bigg\{ F_{y,R,0} + F'_{y,R,0} \Bigg\{ \frac{u[\dot{\beta} + r][m a_F h_{roll}/l + m_s k [1 - f_{roll}] d] + K_R \varphi + D_R \dot{\varphi}}{b_R} - \Delta F_{z,R,0} \Bigg\} \\
& + \Bigg\{ C_{R,0} + C'_{R,0} \Bigg\{ \frac{u[\dot{\beta} + r][m a_F h_{roll}/l + m_s k [1 - f_{roll}] d] + K_R \varphi + D_R \dot{\varphi}}{b_R} - \Delta F_{z,R,0} \Bigg\}\Bigg\} \\
& \times \Bigg[\beta - \frac{a_R}{u} r - \alpha_{R,0}\Bigg]\Bigg\}\Bigg\}
\end{aligned} \tag{A2}$$

$$\ddot{\varphi} = \frac{1}{I_x} \{ m_s u [\dot{\beta} + r] d [1 - k] + m_s g d \varphi - [K_F + K_R] \varphi - [D_F + D_R] \dot{\varphi} \} \tag{A3}$$